Investigations of electronic and optical sources in the mid infrared and terahertz regions

A Dissertation presented

by

Thakur Siddharth Singh

to

The Graduate School

in Partial Fulfillment of the

Requirements

for the Degree of

Doctor of Philosophy

in

Electrical Engineering

Stony Brook University

December 2016

Stony Brook University

The Graduate School

Thakur Siddharth Singh

We, the dissertation committee for the above candidate for the

Doctor of Philosophy degree, hereby recommend

acceptance of this dissertation

Ridha Kamoua - Dissertation Advisor
Associate Professor, Department of Electrical and Computer Engineering

Dmitri Donetski - Chairperson of Defense
Associate Professor, Department of Electrical and Computer Engineering

Leon Shterengas
Associate Professor, Department of Electrical and Computer Engineering

Thomas Cubaud
Associate Professor, Mechanical Engineering

This dissertation is accepted by the Graduate School

Charles Taber
Dean of the Graduate School

For Ammamma, Tata and Daddy.

Acknowledgements

I would like to thank my advisor Professor Ridha Kamoua for all the support and encouragement he has given me during my doctoral studies. He has enabled me to research topics which were of great interest to me and this thesis would not have been possible without him. I hope this thesis is a logical extension of his own Ph.D thesis from Ann Arbor, MI and his knowledge in fabricating and simulating high frequency Gunn oscillators has been invaluable to me. I would also like to thank my host and advisor at Mitsubishi Electric Research Labs, Dr. Keisuke Kojima, for inviting me to work in Cambridge, MA on optical waveguides. My internship under Kojima-san was a very rewarding experience. A special thank you to Professor Wendy Tang for managing my GA time reports. I would also like to thank all the staff in the department for helping me with all the paperwork and documents.

I would never have studied semiconductor devices were it not for my aunt Jayathi. The summers spent with her learning Linux, C programming and numerical methods were my formative steps into research and her husband Sanjay helped me with all my Linux queries. My "American" dad Ramesh uncle kept me enthralled by quoting verbatim, famous quotations from the books he read and passing them of as his. He is the warmest person I know. I would like to thank my dear mother, Deepthi aunty and my good friend Lena for providing me with support and encouragement during my stay in Stony Brook. The dreary winters of Stony Brook would have been unbearable without their phone calls. Lastly, I would like to thank Jihyun for her companionship over the last two years.

Abstract of the Dissertation

Investigations of electronic and optical sources in the mid infrared and terahertz regions

by

Thakur Siddharth Singh

Doctor of Philosophy

in

Electrical Engineering

Stony Brook University

2016

Fundamental sources of mid-infrared and terahertz radiation are of the utmost importance for applications such as chemical sensing, molecular spectroscopy, imaging and telecommunications to name a few. Practical realizations of room temperature fundamental sources in the terahertz region are often hampered by low power and poor temperature performance and this is referred to as the Terahertz gap. This work presents investigations of Quantum Cascade Lasers (QCL) as optical sources of mid-infrared radiation and the proposal of a novel electronic oscillator in the extremely important terahertz region based on a single layer of a suspended graphene sheet.

Monte Carlo simulations of electron and photon transport have been performed on both device concepts. Firstly, the transport models were validated by simulating existing devices from other research groups which have been fabricated and tested. The simulation results of the Monte Carlo model were shown to be in good agreement with experimental data. An injectorless and compact QCL design was proposed. Simulations showed enhanced optical gain, improved temperature performance and very stable and low threshold current densities over a wide temperature range over conventional QCL designs.

A new type of an electronic oscillator based on a single layer of suspended graphene was simulated demonstrating oscillations up to 800 GHz in the terahertz region of the electromagnetic spectrum at room temperature. The proposed device concept could potentially provide a much needed fundamental source in the terahertz region.

Contents

List of Figures

List of Tables

Nomenclature

Physical constants and Global functions

e	Single electron charge: 1.6 x 10^{-19} C
m_0	Free electron mass: 9.1 x 10^{-31} kg
h	Planck's constant: 6.6261 x 10^{-34} J-s
$\hbar$	Reduced Planck's constant: 1.054 x 10^{-34} J-s
k_B	Boltzmann constant: 1.38x10^{-23} J/K
m^*	electron effective mass
v_F	Fermi velocity: 10^6 m/s
$\delta(x)$	Dirac delta function
$\Theta(x)$	Heaviside step function
i or j	: $\sqrt{-1}$

Scattering rate constants

$\hbar\omega_{LO}$	Longitudinal optical phonon energy
$\hbar\omega_0$	Optical phonon energy
T_L	Lattice temperature
ϵ_0	vacuum permittivity: 8.85x10^{-12} F/m

ϵ_∞	High frequency dielectric constant
ϵ_0	low frequency dielectric constant
q_s	Screening length
D_{ac}	Acoustic phonon deformation potential
D_0	Optical deformation potenial
ρ or ρ_m	Mass density
v_s	velocity of sound in material
Δ	Mean roughness height
Λ	Correlation length
ΔV_{ad}	Alloy disorder potential

Chapter 1

Introduction

The design, operation and realization of fundamental sources of mid-infrared (MIR) and terahertz (THz) radiation are active areas of research as they are indispensable components for many important applications. The region comprising wavelengths between 3-12 μm broadly comprises the MIR region of the electromagnetic spectrum and is called the molecular fingerprint region as most of the fundamental rotational and vibrational transitions of the molecular species are located in this region. An illustration of the location of these bands and the various applications that would need MIR sources is shown in Fig. 1.1. One of the most promising and tunable sources of MIR radiation are quantum cascade lasers (QCLs) [2].

Fundamental THz sources are needed for numerous applications as well. THz radiation offers intriguing and exciting possibilities for material and device characterization [3]. Fig. 1.2 illustrates the imaging of a single transistor and the immense improvement in the resolution of the transistor when a THz source is used [3]. In addition to high resolution imaging, the modulation of the output of THz sources is important for high speed communications. Compact THz sources are desirable for high-capacity and short-distance wireless communications [4]. Further motivations for MIR and THz sources will be outlined in subsequent chapters.

The challenges facing designing long wavelength MIR QCLs are principally the waveguide losses which are proportional to the square of the wavelength which limit the optical gain and consequently the power. The increased waveguide losses at longer wavelengths also require larger pumping

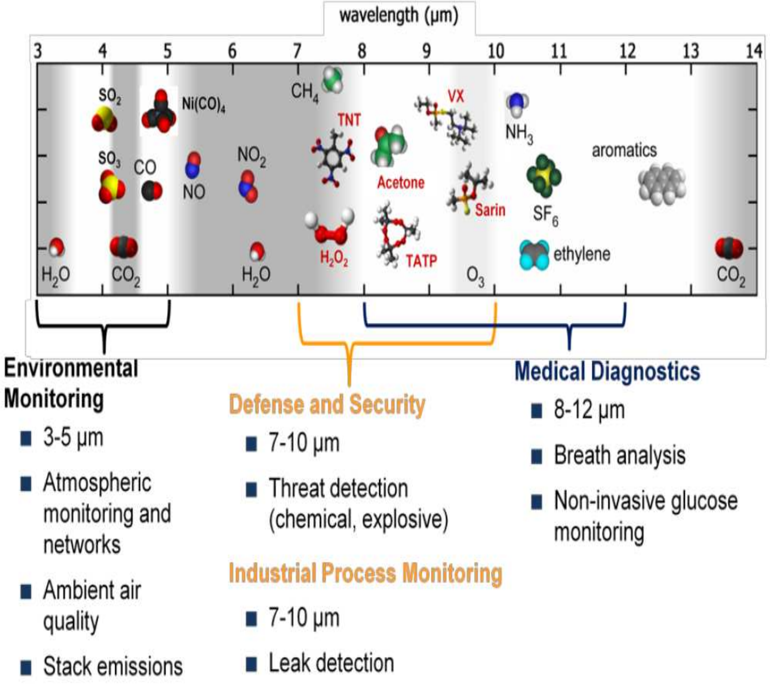

Figure 1.1: Chart showing the location of the strongest rotational vibrational bands for several species based on simulated spectra [1].

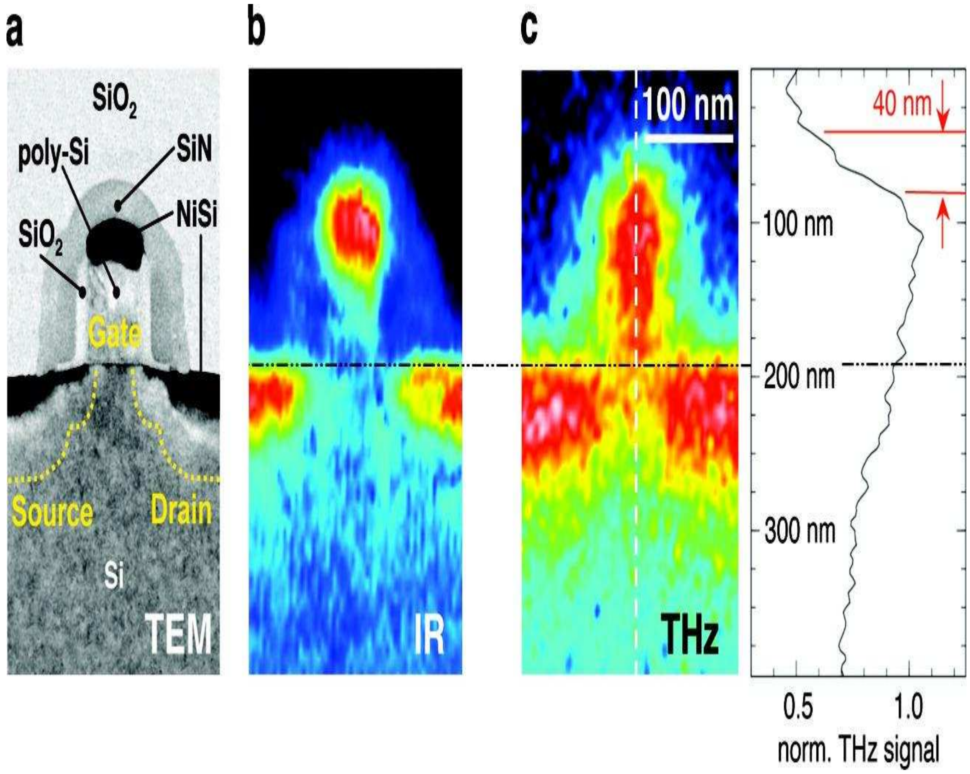

Figure 1.2: TEM image, IR image and high resolution THz image of a single transistor [3].

currents which tend to heat the active region and require extensive cooling. On the other hand, fundamental sources of THz radiation which could potentially be compact components for many applications have been hard to design. The best performing THz sources in the 0.1-5 THz frequency range are either bulky mixers or very low power and low temperature fundamental sources such as RTDs, Josephson junction devices or THz QCLs to name a few. The aim of this dissertation is to use physics based models to quantitatively describe electron and photon transport and propose novel design architectures using the models both in the MIR and THz regions of the electromagnetic spectrum. Part I of this dissertation develops the Monte Carlo based model used for describing transport in QCLs. This model is then used to propose a novel long wavelength QCL and its performance is compared to existing designs. Part II is aimed at proposing a novel THz oscillator based on an exciting new material, suspended graphene. The Monte Carlo model described in Part I will be adapted to simulate the oscillator in Part II. The dissertation is concluded with possible future work for both the device concepts.

Part I

Long Wavelength Mid Infrared QCL

Chapter 2

Ensemble Monte Carlo method

2.1 Intersubband lasers

Quantum cascade lasers (QCLs) [2] are electrically injected semiconductor heterostructure devices which utilize electronic transitions between conduction band states to emit photons and is therefore referred to as an *intersubband* laser. This idea is quite different from conventional heterostructure laser diodes where the optical transition takes place across the band gap separating the conduction and valence band and are called *interband* lasers. Intersubband lasers are called *unipolar* lasers as only electrons or holes participate in producing a laser which interband lasers utilize both holes and electrons simultaneously and hence are called *bipolar* lasers. QCLs have also been shown to operate in the valence band but the strong valence band anisotropy and heavier effective masses coupled with fabrication difficulties have made electron based QCLs the standard.

A semiconductor heterostructure is formed by joining a sequence of alternating wide band gap and narrow band gap materials and hence quantum well and barrier layers are formed in the growth direction which is usually denoted by z. The plane parallel to the growth direction also called the *in-plane* direction is denoted by x-y. A QCL is formed by periodically repeating a single generic stage or period. Each stage in a QCL is a superlattice, i.e., a multiple well-barrier heterostructure. Quantum confinement leads to a set of discrete energies also referred to as *subbands* and the electron's energy in the z direction E_z is confined to one of these subbands. In the plane of

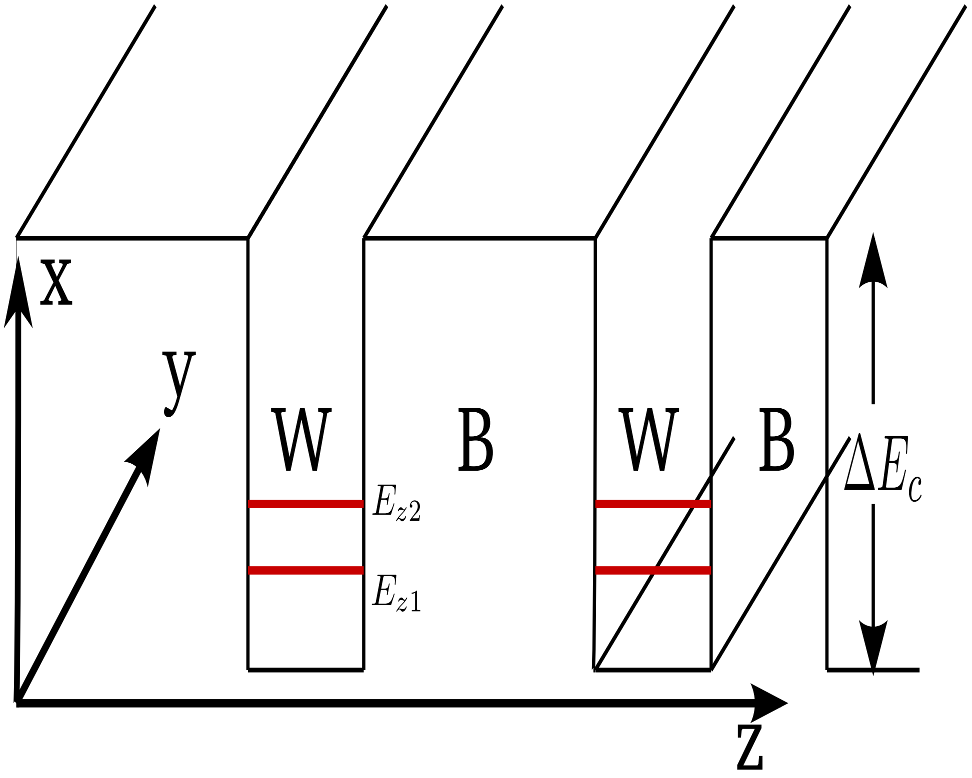

Figure 2.1: Semiconductor heterostructure.

the QCL, the particle feels no confinement and can be thought of as a free electron. A schematic illustration of a semiconductor heterostructure formed in the conduction band is shown in Fig. 2.1.

When an appropriate voltage bias is applied in the z direction, electrons are transported from one stage to another and and with proper wavefunction engineering in the z direction, each electron emits one photon per stage or equivalently N_p photons, where N_p is the number of stages in the QCL. Fig. 2.2 depticts a generic QCL formed by the Γ valley of the conduction band under an applied bias. The length of one stage is L_P. The term cascade in QCL arises from the fact that when a proper bias is applied, electrons continuously lose energy and cascade down an energy staircase emitting a single photon in each stage.

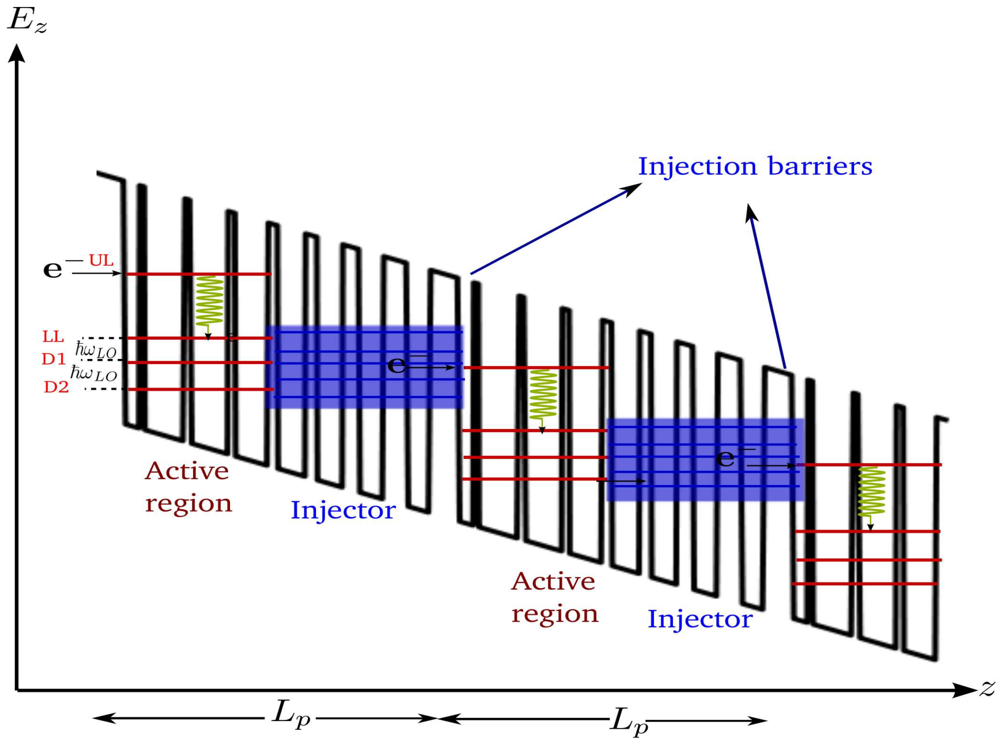

Figure 2.2: Electronic states in a QCL under an applied bias.

2.1.1 Active and Injector regions in a QCL

In Fig. 2.2, the QCL contained two distinct regions namely the active region and the injector region seperated by a thick barrier called the injection barrier. The active region is the portion of the QCL where the optical transition takes place between a upper lasing state UL and a lower laser state LL and this region is usually not doped to avoid carrier absorption induced by photons. The injector region is a set of closely spaced (in energy) subbands which serves the purpose of transporting or injecting the carrier to the next stage. The electrons in the QCL are provided by n-doping certain layers of the injector region. These layers act as electron reservoirs. It is a reasonable assumption that each stage of the QCL is charge neutral, i.e., all the electrons are provided by the doping. To acheive a net gain, one must maintain the population of the UL higher than LL. This is called *population inversion* and it was proposed in 1971 by studying a semiconductor superlattice under an applied electric field [5]. In a QCL this is acheived by engineering levels D1 and D2 which are exactly one optical phonon energy below LL. Thus the lifetime of an electron in LL is very short due to rapid longitudinal phonon emission while the lifetime of an electron in the UL should be as large as possible. The qualitative condition between the population n of a level and lifetime τ for an electron in the level is $n \propto \tau$.

Electron transport in the active region is dictated mainly by longitudinal optical (LO) phonon emission as mentioned before and recently it has been shown that interface roughness (IR) scattering is a crucial transport mechanism. However after threshold when the gain of the laser exceeds the losses of the optical device, stimulated emission plays an exceedingly important part by scattering electrons between the active region subbands. Transport in the injector is a rich interplay between phase coherent tunneling and scattering(also called as incoherent transport). Transport between the active region and injector of a QCL is usually an interplay between coherent and incoherent transport.

2.2 Time dependent Schrödinger equation

The time dependent Schrödinger equation (TDSE) describes the temporal evolution of the quantum state $|\psi(t)\rangle$ of a physical system and is given by,

$$\hat{H}|\psi(t)\rangle = i\hbar\frac{\partial}{\partial t}|\psi(t)\rangle. \tag{2.1}$$

The Hamiltonian of the system describes the various potentials present in the system which give rise to the dynamics of the quantum state. The Hamiltonian of a system can be divided into two components. The first component describes potentials which are time-independent and will be denoted by $\hat{H}_0$ and the second one describes time varying potentials $\hat{V}(t)$. The TDSE can now be written as,

$$(\hat{H}_0 + \hat{V}(t))|\psi(t)\rangle = i\hbar\frac{\partial}{\partial t}|\psi(t)\rangle. \tag{2.2}$$

In one dimensionally confined semiconductor heterostructures such as QCLs, $\hat{H}_0$ generally contains the kinetic energy of an electron $\hat{T}$, the conduction band offset between the constituent materials of the well and barrier regions in the growth or confinement direction of the heterostructure (denoted by z) $E_c(z)$, electric fields due to an applied electric field in the z direction F given by $V_E(z) = -eFz$ and any self consistent Hartree potentials $-e\phi_H(z)$ due to charge redistribution obtained by solving Poisson's equation. Band parameters for most III-V materials and alloys can be found in [24]. The potential in the plane parallel to z(denoted by x-y) is assumed to be constant and uniform. Thus,

$$\hat{H}_0 = \hat{T} + E_c(z) + V_E(z) - e\phi_H(z). \tag{2.3}$$

The time varying potential arises due to various scattering mechanisms such as phonons, interface roughness, alloy disorder, electron-electron and photon induced scattering. These potentials are usually treated as small perturbations to $\hat{H}_0$.

If the eigenstates of the stationary unperturbed system $\hat{H}_0$ are denoted by $|\phi\rangle$ and the eigenenergies E_ϕ correspoding to each $|\phi\rangle$ represent the electron energies as a result of a measurement of electron energy,then the time dependent form of the eigenstates is,

$$|\phi(t)\rangle = |\phi\rangle \exp\left(\frac{-iE_\phi t}{\hbar}\right). \tag{2.4}$$

In the next section we will find the stationary electronic states in a QCL. As the time varying potentials act as small perturbations to $\hat{H}_0$, we can employ perturbation theory to solve for the effects of the time varying potentials. The explicit form of the scattering rates due to the time varying scattering mechanisms along with the details of the solution obtained using perturbation theory will be described in the next chapter.

2.3 Time-independent Schrödinger equation

The time-independent Schrödinger equation (TISE) enables us to calculate the stationary electronic states in a QCL. The TISE is given by,

$$\hat{H}_0|\phi\rangle = E_z|\phi\rangle. \tag{2.5}$$

Here E_z is the quantization energy in the z direction as $\hat{H}_0$ varies only in the z direction.

The three dimensional stationary wavefunction $|\phi\rangle(\mathbf{R})$ is given by the product of a slowly varying component along the quantization direction called the envelope function $\psi(z)$ and a rapidly varying component called the Bloch function $u_{\mathbf{k}}(\mathbf{R})$.

$$|\phi\rangle(\mathbf{R}) = \frac{1}{\sqrt{A}} e^{i\mathbf{k}.\mathbf{r}}\psi(z)u_{\mathbf{k}}(\mathbf{R}) \tag{2.6}$$

where $\mathbf{k}$ is the 2D in-plane or parallel momentum also denoted by $\mathbf{k_{xy}}/\mathbf{k}_{\parallel}$, $\mathbf{r}$ is the in-plane position and A is the cross sectional area in the x-y plane which is the normalization constant.

Under the assumption that the Bloch function does not change spatially when moving from the well to the barrier regions owing to the fact that the constituent materials of the well and barrier regions possess similar crystal structures, the TISE reduces to,

$$\hat{H}_0\psi(z) = E_z\psi(z). \tag{2.7}$$

This ansatz is called the ***envelope function approximation*** [15] and has shown to produce good agreement with more accurate atomistic bandstructure methods.

2.3.1 Non-parabolicity

The kinetic energy operator for a free electron is given by,

$$\hat{T} = -\frac{\hbar^2}{2m^*}\Delta,$$

where m^* is the effective mass of the electron and the $\Delta = \frac{\partial^2}{\partial z^2}$ is the Laplacian operator. This leads to what is called the parabolic Schrödinger equation as such an operator leads to a parabolic relation(also called the $E-k$ dispersion relationship) between the energy and momentum in the plane of the QCL,

$$E = \frac{\hbar^2 k^2}{2m^*}$$

where k is the magnitude of the in-plane momentum.

$$-\frac{\hbar^2}{2m^*}\frac{\partial^2\psi}{\partial z^2} + V_c(z) = E_z\psi(z) \tag{2.8}$$

Here we have combined the conduction band offset, electric field and Hartree potentials into an effective potential $V_c(z)$.

This is however not an accurate description of the electronic states as electrons in the conduction band of a QCL feel the potential due to the remote band electrons such as valence band electrons and to be exact even higher lying conduction bands. This can lead to corrections in the values of the eigenenergies E_z. To accurately solve for the effects of remote bands on the electron states, effective mass theories such as the 8x8 **k.p** method can be employed but they are computationally too expensive to be implemented in a design tool. Therefore to simplify the problem we introduce a factor α called the non-parabolicity factor to describe the effects of the remote bands. We restrict ourselves to the remote valence bands only as this has been shown to produce energies which are in reasonable agreement with experiment. The $E-k$ dispersion though will still be assumed to be parabolic in this work as non-parabolicity manifests itself to greater effect only at higher energies and since there is no electric field in the in-plane direction, we can neglect the corrections to the dispersion relationship.

The non-parabolicity factor is given by,

$$\alpha(z) = \frac{\beta(z)}{E_g(z)}\left(1 - \frac{m^*(z)}{m_0}\right) \tag{2.9}$$

$$\beta(z) = \frac{1 + 4x(z) + 2x^2(z)}{1 + 5x(z) + 2x^2(z)} \tag{2.10}$$

$$x(z) = \frac{\Delta_{so}(z)}{E_g(z)} \tag{2.11}$$

where m_0 is the free electron mass Δ_{so} is the spin orbit split off energy and E_g is the direct band gap. All quantities in the above equation are spatially varying in the z direction to account for the fact that the well and barrier regions in the QCL are composed of different materials. The non-parabolic TISE is now given by,

$$-\frac{\hbar^2}{2}\frac{\partial}{\partial z}\left(\frac{1}{m^*(z)(1+\alpha(z)[E_z - V_c(z)])}\frac{\partial \psi}{\partial z}\right) + V_c(z)\psi(z) = E_z\psi(z). \tag{2.12}$$

This is a non-linear eigenvalue problem and can be converted into a linear eigenvalue problem and solved using the finite difference method [16] to yield the subband quantization energies E_z and the envelope functions $\psi(z)$. A detailed derivation and description of this solver will be given in Appendix A. The total energy of an electron E_ϕ is given by,

$$E_\phi = E_z + \frac{\hbar^2 k^2}{2m^*}. \tag{2.13}$$

Here m^* can be taken to be the effective mass in the well.

A QCL is a periodic repetition of a single stage of length L. To reflect the correct boundaries at the beginning and end of each stage, we solve the non-parabolic TISE over three periods with the boundary conditions $\psi(0) = 0$ and $\psi(3L) = 0$ and we take the central period states as the correct ones. Owing to the translational invariance of the QCL, we can calculate the wavefunctions in any other stage of the QCL by appropriate shifts in space and energy of the central period states. In the next few sections, a detailed procedure for calculating the conduction band offsets will be given and then a method for incorporating the self-consistent potential will be detailed.

2.4 Conduction band offsets

An excellent and thorough review of the material parameters for commonly used III-V alloys and materials was published in [24]. The QCLs considered in this thesis were electron based conduction band QCLs and therefore it is necessary to have a quantitative framework for calculating the conduction band offsets of these material systems and the method adopted in [33] is followed.

In order to calculate the conduction band offsets, one needs to know the value of the valence band offset parameter (VBO), since the valence band offsets have been studied much more extensively. The convention that is usually adopted is to find the parameter VBO, which is the valence band offset relative to a pre-determined reference material whose VBO is specified. In [24], for example, VBO(InSb)=0 has been adopted. Hence, the VBO for any two materials is found as the difference in VBO of the two materials under consideration. In order to calculate the conduction band offset, one simply needs to add the band gap of each material to its respective VBO. The conduction band edge or minimum (at the Γ point to be precise) is called ${E_c}^\Gamma$ and can be computed using the following equation,

$$ {E_c}^\Gamma = VBO + {E_g}^\Gamma + \delta E_{Vars} + \delta E_{c\epsilon} + \delta E_{v\epsilon}, \tag{2.14} $$

where ${E_g}^\Gamma$ is the band gap at the Γ point at T=0 K, δE_{Vars} is the Varshney correction to the band gap energy at non-zero temperatures, and $\delta E_{c\epsilon}$ and $\delta E_{v\epsilon}$ are the strain induced corrections to the conduction and valence band edges due to deformation. The conduction band offset for a heterostructure formed by two arbitrary materials A and B is therefore simply the difference in the energies of their conduction band edges and is given by,

$$ \Delta {E_c}^\Gamma = {E_c}^\Gamma(A) - {E_c}^\Gamma(B). \tag{2.15} $$

A ternary alloy is a material whose chemical composition can be written in the form $A_x B_{1-x} C$ and is composed of its two constituent binaries $(AC)_x$ and $(BC)_{1-x}$. x is the mole fraction and can range between 0 and 1. Thus any parameter P of the ternary alloy can interpolated as the mole fraction weighted average of the parameters of its constituent binaries. The material parameters for the binary alloys InAs, GaAs and AlAs which are commonly

Table 2.1: Material parameters for InAs, GaAs and AlAs

Parameter	InAs	GaAs	AlAs
a_l (A^o)	6.0583	5.6533	5.6611
c_{11} (GPa)	832.9	1221	1250
c_{12} (GPa)	452.6	566	534
${E_g}^{\Gamma}$ (eV)	0.417	1.519	3.099
Δ_{SO} (eV)	0.39	0.341	0.28
VBO (eV)	-0.59	-0.80	-1.33
${a_c}^{\Gamma}$ (eV)	-5.08	-7.17	-5.64
a_v (eV)	-1	1.16	-2.47
b (eV)	-1.8	-2.0	-2.3
E_P (eV)	21.5	28.8	21.1
F	-2.90	-1.94	-0.48
${m_e}^{\Gamma}/m_0$	0.026	0.067	0.15
α^{Γ} (meV/K)	0.276	0.5405	0.885
β^{Γ} (K)	93	204	530
ϵ_s	14.3	12.9	10.06
ϵ_∞	11.6	10.86	8.16
$\hbar\omega_{LO}$	29.93	35.3	49.8

used binaries for the heterostructure alloys of mid infrared QCLs are given in Table 2.1 and are taken from [24].

$$P(A_xB_{1-x}C) = xP(AC) + (1-x)P(BC) + C_Bx(1-x) \tag{2.16}$$

Here C_B is called the bowing factor and is a characteristic of the ternary alloy. There are uncertainties in the determination of C_B often and in these cases, a zero bowing factor $C_B = 0$ is assumed. The bowing parameters are given in Table 2.2

2.4.1 Varshney corrections

The temperature dependence of the band gap is given in terms of the two Varshney parameters α and β and is given by,

$$E_g(T) = E_g(0) - \frac{\alpha T^2}{\beta + T}. \tag{2.17}$$

Table 2.2: Bowing parameters for InGaAs and InAlAs

Parameter	InGaAs	InAlAs
${E_g}^{\Gamma}$ (eV)	0.477	0.70
Δ_{SO} (eV)	0.15	0.15
VBO (eV)	-0.38	-0.64
E_P (eV)	-1.48	-4.81
F	1.77	-4.44
${m_e}^{\Gamma}/m_0$	0.0091	0.049
${a_c}^{\Gamma}$ (eV)	2.61	1.4

Thus, the Varshney correction factor is,

$$\delta E_{Vars} = -\frac{\alpha T^2}{\beta + T}. \tag{2.18}$$

2.4.2 Strain induced corrections

Semiconductor epitaxy is used to grow the heterostructures used in QCLs. The grown materials often have lattice constants different from that of the substrate material. As can be imagined, strain is undesirable and the accumulation of strain leads to epitaxial defects. Since the lattice constant and band gap are functions of the mole fraction x, the only way to alter the material band gap is to change x and thereby induce strain. Thus, all the grown materials need not be lattice matched to the substrate. The ability to vary x, vary material compositions and intentionally induce strain allows one to tailor the conduction band offset depending on the desired design wavelength.

However, it is possible to achieve "strain balancing" by inducing compressive strain in one layer while tensile strain in the other layer of the heterostructure. This is referred to as a "strain balanced heterostructure". Most III-V alloys crystallize under the zinc blende structure which has cubic symmetry. These alloys acquire biaxial strain when grown epitaxially on a substrate with a different lattice constant. This means that only the diagonal components of the three dimensional strain tensor are non-zero. If z is the the direction of epitaxial growth, a_0 the lattice constant of the substrate and

a_l the lattice constant of the epitaxial layer, then,

$$\epsilon_{xx} = \epsilon_{yy} = \frac{a_0 - a_l}{a_l}; \epsilon_{zz} = -\frac{2c_{12}}{c_{11}}\epsilon_{xx}. \tag{2.19}$$

c_{11} and c_{12} are the elastic stiffness constants of the layer material. Strain effects on the bandgaps of semiconductors have been modeled using the Pikus-Bir interaction [34] and Van de Walle "model solid" theory [35]. The relative change in volume V due to strain is related to the change in the band gap by a hydrostatic deformation potential a.

$$\frac{\delta V}{V} = \epsilon_{xx} + \epsilon_{yy} + \epsilon_{zz} \tag{2.20}$$

$$\delta E_\epsilon = a\frac{\delta V}{V} \tag{2.21}$$

The components of this correction or shift acquired by the conduction band and valence bands are,

$$\delta E_{\epsilon c} = a_c\frac{\delta V}{V}; \delta E_{\epsilon v} = a_v\frac{\delta V}{V} \tag{2.22}$$

where a_c and a_v are the conduction and valence band hydrostatic deformation potentials and are related to a by $a = a_c + a_v$. Compressive strain adds hydrostatic pressure and increases the band gap. This can be visualized as the moving up of the conduction band edge by a_c/a and the moving down proportionally of the valence band edge by a_v/a.

The light hole (LH), heavy hole (HH) and split-off (SO) valence bands have a p-state shape and therefore lack spherical symmetry unlike the conduction band (C) which has a s-state shape. Due to this asymmetry in the valence bands, the biaxial strain in the valence bands has a shear component that splits the degeneracy of the HH and LH bands. Using the Bir-Pikus Hamiltonian [34], the energy band gaps with shear strain including the spin-orbit interaction are,

$$E^{\Gamma}{}_{C-HH} = E_g{}^{\Gamma} + \delta E_{\epsilon c} + \delta E_{\epsilon v} - Q_\epsilon \tag{2.23}$$

$$E^{\Gamma}{}_{C-LH} = E_g{}^{\Gamma} + \delta E_{\epsilon c} + \delta E_{\epsilon v} + \frac{1}{2}(Q_\epsilon - \Delta_{SO} + \sqrt{\Delta_{SO}{}^2 + 2\Delta_{SO}Q_\epsilon + 9Q_\epsilon{}^2}), \tag{2.24}$$

$$E^{\Gamma}{}_{C-HH} = E_g{}^{\Gamma} + \delta E_{\epsilon c} + \delta E_{\epsilon v} - \frac{1}{2}(Q_\epsilon - \Delta_{SO} - \sqrt{\Delta_{SO}{}^2 + 2\Delta_{SO}Q_\epsilon + 9Q_\epsilon{}^2}), \tag{2.25}$$

where Δ_{SO} is the split-off energy and the shear deformation potential b is included in Q_ϵ which is given by,

$$Q_\epsilon = \frac{b}{2}(\epsilon_{xx} + \epsilon_{yy} - 2\epsilon_{zz}). \tag{2.26}$$

2.5 Poisson's equation

In order to update the electric field to account for space charge effects and add a self-consistent potential to the TISE, Poisson's equation is solved using a standard centralized finite difference scheme. Poisson's equation takes the form,

$$\frac{\partial}{\partial z}(\epsilon(z)\frac{\partial \phi_H}{\partial z}) = -e(N_d(z) - n_e(z)), \tag{2.27}$$

where ϕ_H is the self-consistent Hartree potential across the device. ϵ, N_d and n_e are the effective permittivity, doping profile and electron densities in the device respectively and all are spatially varying quantities in the growth direction z.

The electron density in a QCL can be calculated in the following manner,

$$n_e(z)_= \sum_{j=1}^{N_{sub}} n_j |\psi_j(z)|^2, \tag{2.28}$$

where N_{sub} is the number of subbands in the QCL, n_j is the sheet density of the jth subband described by the wavefunction $\psi_j(z)$. The numerical method used to solve Poisson's equation will be now be detailed.

Poisson's equation can be written more succinctly by defining an effective charge density $\rho(z) = -e((N_d(z) - n_e(z))$ and for convenience dropping the subscript H in the Hartree potential $\phi_H(z)$ as,

$$\frac{\partial}{\partial z}(\epsilon(z)\frac{\partial \phi}{\partial z}) = \rho(z), \tag{2.29}$$

Let L be the length of the domain in which Poisson's equation is to be solved. A grid is created in the z direction and let the grid be discretized with a step δz into N_z points with $i = 1, 2, 3...N_z$ being the index labelling the grid points $\delta z, 2\delta z, 3\delta z...N_z\delta z$ (L=$N_z\delta z$). Boundary conditions of $\phi(0) = 0$ and $\phi(L) = \phi_L$ are assumed with ϕ_L being the desired potential at the end point of the domain. The finite difference approximation of the second order partial derivative (see Appendix D) is,

$$\phi_{i-1}(\epsilon_i + \epsilon_{i-1})/2 - \phi_i(\epsilon_i + (\epsilon_{i-1} + \epsilon_{i+1})/2) + \phi_{i+1}(\epsilon_i + \epsilon_{i+1})/2 = \delta z^2 \rho_i \tag{2.30}$$

This is a purely tri-diagonal matrix equation and can be rapidly solved using the Thomas algorithm which is also referred to as the TDMA [68]. For devices with a uniform dielectric constant, i.e., $\epsilon_{i\pm1} = \epsilon_i$, Eq. (2.30) simplifies to,

$$\phi_{i-1} - 2\phi_i + \phi_{i+1} = \frac{\delta z^2 \rho_i}{\epsilon_i}. \tag{2.31}$$

2.6 Scattering rates in QCLs

The various rates due to the scattering mechanisms which transport the electrons between the subbands of a QCL will now be described and are calculated using Fermi's golden rule which is described in Appendix B. The numerical methods for computing the integrals describing the following scattering rates can be found in Appendix D.

2.6.1 Longitudinal optical phonon scattering

The scattering rate due to the emission(ems) or absorption(abs) of a longitudinal phonon by an electron initially in subband i with an in-plane momentum k_i and envelope function $\psi_i(z)$ making a transition to subband f and envelope function $\psi_f(z)$ is given by [19],

$$\frac{1}{\tau_{if}}^{LO}(\mathbf{k_i}) = \frac{m^* e^2 \hbar \omega_{LO}}{8\pi \hbar^3 \epsilon_0}({\epsilon_\infty}^{-1} - {\epsilon_0}^{-1}) \left[N_{LO} \int_0^{2\pi} M_{if}(q_{abs}) d\theta + (N_{LO}+1) \int_0^{2\pi} M_{if}(q_{em}) d\theta \right] \tag{2.32}$$

where ω_{LO} is the angular frequency of a longitudinal optical phonon and θ is the angle between k_i and k_f. N_{LO} is the equilibrium phonon occupation number and is given by Bose-Einstein statistics

$$N_{LO} = \frac{1}{\exp(\frac{\hbar\omega_{LO}}{k_B T_L}) - 1}, \tag{2.33}$$

$$M_{if}(q) = \int dz \int dz' \rho_{if}(z) {\rho^*}_{if}(z') I(q, q_s, z, z'), \tag{2.34}$$

$$\rho_{if}(z) = {\psi^*}_i(z)\psi_f(z), \tag{2.35}$$

$$I(q, q_s, z, z') = \frac{e^{-\sqrt{q^2+{q_s}^2}|z-z'|}}{\sqrt{q^2+{q_s}^2}} \left[1 - \frac{|z-z'|{q_s}^2}{2\sqrt{q^2+{q_s}^2}} - \frac{{q_s}^2}{2(q^2+{q_s}^2)}\right], \tag{2.36}$$

$$q_{em,abs}(\theta) = \sqrt{2{k_i}^2 - 2\frac{m^*\Delta E_{abs,ems}}{\hbar^2} - 2k_i cos(\theta)\sqrt{{k_i}^2 - 2\frac{m^*\Delta E_{abs,ems}}{\hbar^2}}}, \tag{2.37}$$

$$\Delta E_{abs,ems} = E_f - E_i \mp \hbar\omega_{LO}. \tag{2.38}$$

2.6.2 Acoustic deformation phonon scattering

The $\omega - k$ dispersion relationship for the acoustic phonon branch can be approximately considered to be linear. Using deformation potential theory, the scattering rates due to acoustic phonons is given by [18],

$$\frac{1}{\tau_{if}}^{ADP}(\mathbf{k_i}) = \frac{m^* D_{ac} k_B T_L}{\hbar^3 \rho {v_s}^2} \int dz {\psi_f}^2(z){\psi_i}^2(z). \tag{2.39}$$

2.6.3 Interface roughness scattering

In reality, heterostructures are not perfectly flat and random fluctuations in the interface location cause small shifts in the conduction band offset and this acts as a scattering potential for the electrons as they traverse the QCL. It is now widely accepted that interface roughness scattering is crucial in understanding the operation of a QCL. The scattering rate due to roughness assuming perfectly abrupt interfaces is given by [18],

$$\frac{1}{\tau_{if}}^{IR}(\mathbf{k_i}) = \sum_I \frac{m^* \Delta^2 \Lambda^2 |F_{if,I}|^2}{\hbar^3} \int_0^\pi e^{-\Lambda^2 {q_\alpha}^2/4} d\theta, \tag{2.40}$$

$${q_\alpha}^2 = 2({k_i}^2 + \frac{m^* E_{if}}{\hbar^2} - k_i \sqrt{{k_i}^2 + 2\frac{m^* E_{if}}{\hbar^2} cos(\theta)}), \tag{2.41}$$

$$F_{if,I} = V(z_I) {\psi^*}_i(z_I) \psi_f(z_I). \tag{2.42}$$

Δ, Λ are the mean roughness height and correlation length for the interfaces respectively and $V(z_I)$ is the potential jump at the I^{th} interface.

2.6.4 Alloy disorder scattering

The constituent materials of the well and barrier regions of the QCL are alloys. The atoms comprising the alloys are distributed randomly in the alloy and the crystal potential due to this randomness varies stochastically. To overcome this difficulty, the model solid approximation was proposed where the random atoms were replaced by a uniform array of atoms. Although the virtual crystal model matches the average potential, microscopic fluctuations on the atomic scale act as perturbations to the electrons and manifest themselves as a scattering rate given by [18],

$$\frac{1}{\tau_{if}}^{AD}(\mathbf{k_i}) = \frac{m^* a^3 {\Delta V_{ad}}^2}{8\hbar^3} x(1-x) \int dz |\psi_i(z)|^2 |\psi_f(z)|^2. \tag{2.43}$$

a is the lattice constant, x and $1-x$ are the mole fractions of the compounds making up the alloy and ΔV_{ad} is the alloy disorder potential.

2.6.5 Optical cavity dynamics and Photon induced scattering

The scattering due to the emission and absorption of photons is an important scattering mechanism when the QCL is lasing. This scattering rate between any two subbands in calculated in the following manner [26].

The Number of photons in a laser mode is,

$$\frac{n_0}{c}\frac{dN_m}{dt} = (\Gamma g_m - a(\omega_m))N_m, \tag{2.44}$$

with the gain in each mode m being,

$$\mathbf{g_m} = \frac{\pi\omega_\mathbf{m}\mathbf{Z_0}}{\mathbf{V}\mathbf{n_0}\hbar}\sum_\mathbf{p}\sum_\mathbf{f}\frac{\omega_{\mathbf{i_p},\mathbf{f}}}{|\omega_{\mathbf{i_p},\mathbf{f}}|}|\mathbf{d_{i_pf}}|^\mathbf{2}\mathcal{L}_\mathbf{i_pf}(\omega_\mathbf{m}). \tag{2.45}$$

The optical Mode intensity is given by,

$$I_m(\omega_m) = \frac{\Gamma N_m\hbar\omega_m c}{V_g n_0}. \tag{2.46}$$

The optical mode dynamics are,

$$\frac{dI_m}{dt} = \frac{c}{n_0}(\Gamma g_m - a(\omega_m))I_m, \tag{2.47}$$

and at steady state, $\frac{dI_m}{dt} = 0$ leading to the gain=loss condition, i.e., $g = \frac{a}{\Gamma}$. The time evolution for the mode intensity I_m can be found by integrating Eq. (2.47). Assuming the initial mode intensity at $t = 0$ at the beginning of the simulation to be I_0 (which can be 0 or any arbitrarily small intensity such as 1000 W/cm^2), the intensity at any non-zero time t is,

$$I_m(t) = I_0\exp(\frac{c}{n_0}(\Gamma g_m - a(\omega_m))t). \tag{2.48}$$

Finally experimentally measurable parameters such as power and the wall plug efficiency can be be calculated using,

$$P_m = 0.5I_mA(1-R)/\Gamma; WPE = \frac{P_m}{VI}. \tag{2.49}$$

The semiclassical rate induced due to stimulated photon processes is,

$$\left(\frac{1}{\tau_{if}}\right)^{h\nu}(k_i) = \frac{\pi Z_0}{n_0\hbar^2}|d_{if}|^2\sum_m I_m\mathcal{L}_{if}(\omega_m). \tag{2.50}$$

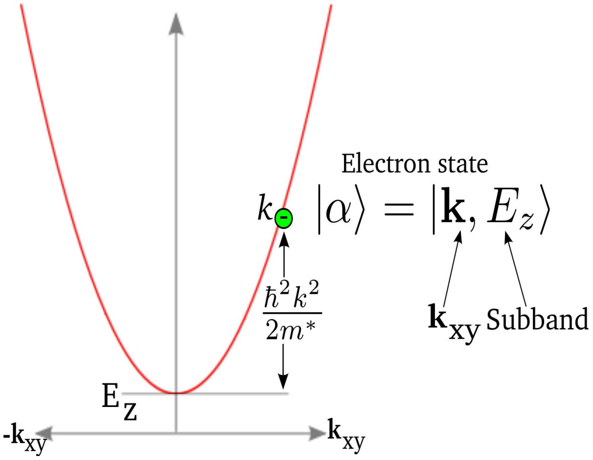

Figure 2.3: The state of an electron $|\alpha\rangle$ in a subband of a QCL.

2.7 Boltzmann-like transport equation for QCLs

An electron in the Γ valley of the QCL is characterized by the state $|\alpha\rangle$ $= |\mathbf{k}, E_z, S\rangle$ where $\mathbf{k} = \sqrt{{k_x}^2 + {k_y}^2}$ is the 2D wave vector in the parallel plane, E_z is the energy of the subband in the quantized (z) direction and S is the stage/period of the QCL. The state of an electron in a QCL is illustrated in Fig. 2.3. The time evolution of the electron distribution function f_α (neglecting coherences and assuming that the cell periodic Bloch functions are the same in the well and barrier regions) which gives us the probability that an electron is in a state $|\mathbf{k}, E_z, S\rangle$ at time t is given by [21],

$$\frac{df_\alpha}{dt} = \sum_{\mathbf{k}', {E_z}', S'} \left\{ P_{{E_z}'S', E_zS}(\mathbf{k}', \mathbf{k}) f_{\alpha'}(t)(1 - f_\alpha(t)) - P_{E_zS, {E_z}'S'}(\mathbf{k}, \mathbf{k}') f_\alpha(t)(1 - f_{\alpha'}(t)) \right\}. \tag{2.51}$$

Here P is the total scattering rate for an electron to make a transition from the state $|\alpha\rangle$ to $|\alpha'\rangle$ and is qualitatively given by Matthiessen's rule,

$$P = \frac{1}{\tau}^{LO} + \frac{1}{\tau}^{ADP} + \frac{1}{\tau}^{IR} + \frac{1}{\tau}^{AD}. \tag{2.52}$$

(2.51) is basically the celebrated Boltzmann transport equation (BTE) and is one of the cornerstones of non-equilibrium statistical mechanics. Semiconductor device physicsits have used the BTE for nearly half a century now to study charge transport. There is however an important difference between (2.51) and the standard BTE. The absence of an electric field in the plane of QCL leads to an absence of the drift and diffusion terms of the BTE. Also, the electric field in the z direction doesn't explicitly accelerate the electrons but by modifying the envelope wavefunctions $\psi(z)$ affects the scattering rates and hence the electron transport.

2.7.1 Solving the BTE

The BTE is a complex integro-differential equation and analytical solutions are rarely possible. The relaxation time approximation is one of the few examples where an analytical solution to the BTE has been found but it is valid only for situations where the device is not far from equilibrium. The BTE has resisted analytical attacks for years now and the best bet is to search for a numerical solution. The two most popular numerical methods for solving the BTE were presented in the 1966 Kyoto semiconductor conference and are the Monte Carlo method (Kurosawa) and the iterative method(Budd). The Monte Carlo method is by far the more popular of the two because of it's physical intuitiveness and ease of use. The Monte Carlo method for solving the BTE will now be described.

2.7.2 Physical interpretation and validity of the BTE

The BTE has a very simple yet powerful interpretation. It tell us that the net incoming flux of electrons into a state $|\alpha\rangle$ should equal to the net outgoing flux from $|\alpha\rangle$ to all other states $|\alpha'\rangle$ once steady state has been reached $\frac{df_\alpha}{dt} = 0$. This is schematically illustrated in Fig. 2.4.

The physical mechanisms that govern the fluxes are essentially the scattering rates we have described in the section. Mathiessen's rule which was briefly mentioned will now be explained in greater detail for QCLs keeping in mind the fact that a QCL is a multisubband system and therefore an electron in a particular state would have many possible scattering paths. Before we continue, it is worth mentioning the the approximations inherent in the BTE. The salient points to remember are,

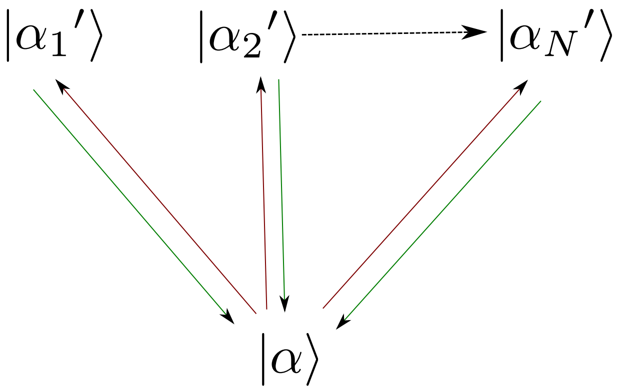

Figure 2.4: The total incoming flux represented by the green arrows must equal the total outgoing flux represented by the red arrows at steady state.

- 1. Scattering processes are instantaneous in space and time.
- 2. Scattering processes are uncorrelated, i.e. ,they are independent of previous scattering events. This is called the Markov approximation.
- 3. The distribution function is a single electron distribution function and multi electron correlations are neglected. This assumption is somewhat relaxed when including electron-electron scattering.

Based on these assumptions we will now outline the theory behind the ensemble Monte Carlo method for solving the BTE.

2.8 Implementation of the Ensemble Monte Carlo simulator

The semiclassical ensemble Monte Carlo method (EMC) is a powerful stochastic technique which has been employed by device physicists and engineers for nearly half a century to simulate nonequilibrium transport in semiconductor devices [20, 21, 22, 23]. It has found remarkable success in explaining physical phenomena hardly accessible to experiment. Physically important macroscopic parameters such as electron mobility, diffusion coefficients, drift velocity and thermal conductivity to name a few and even microscopic quantities such as the electron distribution function, electron temperature and charge distributions can be readily obtained as outputs of the EMC method [22]. The flowchart of the EMC algorithm is first illustrated in Fig. 2.5 and each individual step in the EMC will be explained in detail.

In the EMC, a random walk is generated to simulate the stochastic motion of electrons subject to the scattering mechanisms outlined in the previous chapter. This in essence is equivalent to the random walk sampling technique used in the evaluation of multi-dimensional integrals. The basic idea is to simulate the free flight of an electron followed by an instantaneous scattering process. The free flight is the time duration after which the scattering process takes place and is related to the lifetime of the electron. The EMC algorithm consists of generating random free flight times for a simulated ensemble of electrons N_{sim} usually between $10,000$ to $15,000$ which represent a sample of the doping, choosing the type of scattering terminating the free flight, updating the energy and momentum of the electron based on the scattering mechanism and then repeating the procedure for all the simulated electrons until a steady state has been reached. Sampling the electron motion at various instances of time allows for the statistical estimation of the physical parameters of the device.[23].

The EMC simulator consists of the following steps.

- The conduction band offset for a given heterostructure is calculated using the framework detailed in section 2.4.
- The electronic states are solved using Eq. (2.12) resulting the stationary wavefunctions and their respective discrete energy levels along the growth or z direction.
- The scattering rates between the various states are calculated using the equations from section 2.6.
- An ensemble of electrons or particles is initialized according to a Maxwellian distribution at the operating temperature of the device.
- The particles are dynamically tracked in time steps and perform a series of free flights and undergo scattering events at the end of each free flight.

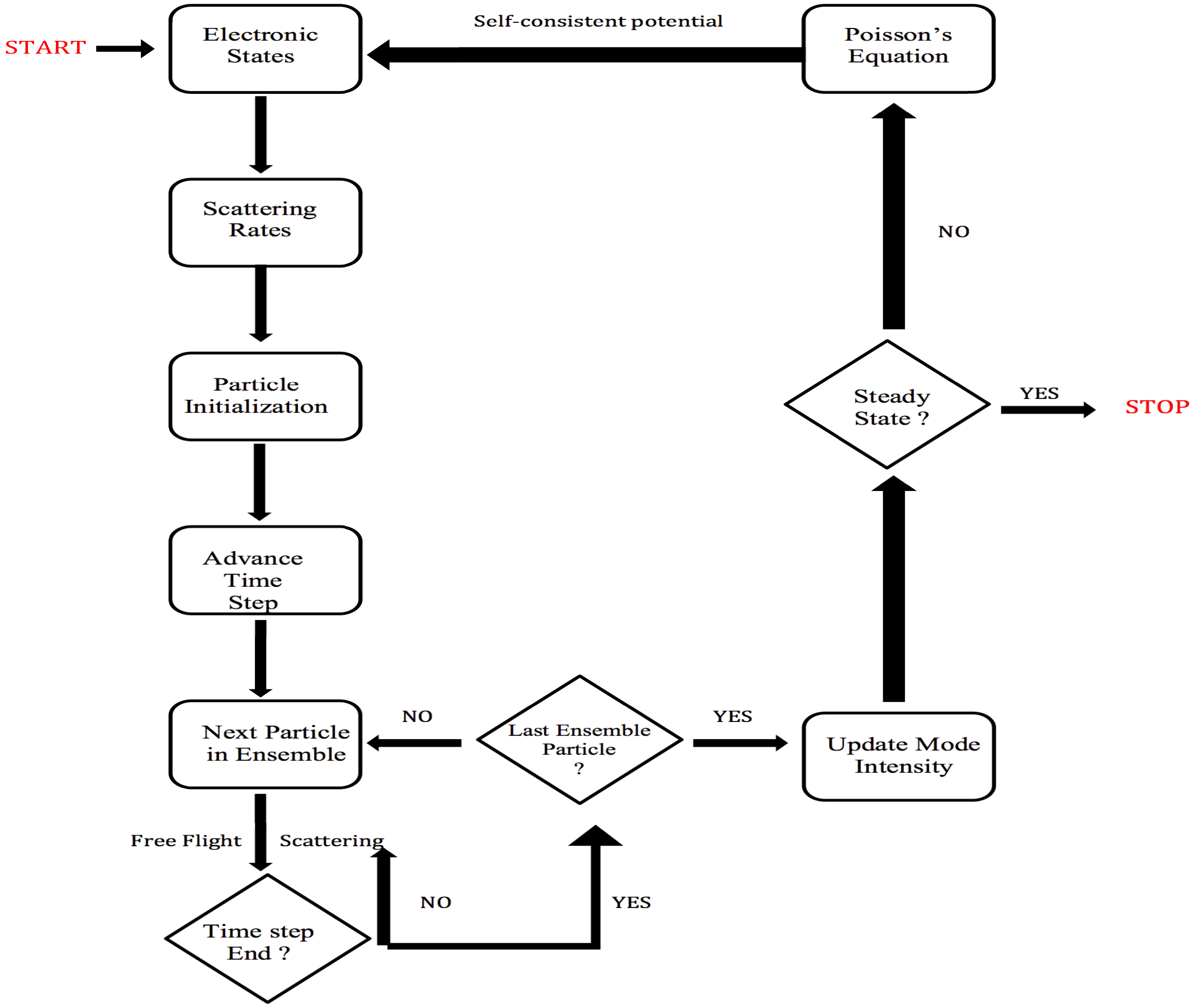

Figure 2.5: The flowchart of the EMC method.

- The energy and momentum of each particle is updated according to the scattering event which occurs.
- At the end of each time step, the mode intensities are updated according to the framework presented in section 2.6.5.
- In addition, Poisson's equation can be solved using the method detailed in section 2.5.
- The simulation is completed when the ensemble averaged observables reach their respective steady states.

Detailed descriptions of the generation of free flights and scattering event updates using random numbers will now be given.

2.8.1 Free flight

The $lifetime$ of an electron in a state addressed by it's subband i and in-plane momentum $\mathbf{k_i}$ denoted by $\Gamma_i(\mathbf{k_i})$, is related to the total scattering rate which transports the electron from this state to all other possible final states f. If the reciprocal scattering rate or lifetime for an electron with subband i and in-plane momentum $\mathbf{k_i}$ to make a transition to subband f due to a scattering mechanism *scatt* is denoted by,

$$\Gamma^{scatt}{}_{if}(\mathbf{k_i}) = \frac{1}{\tau_{if}}^{scatt}(\mathbf{k_i}) \tag{2.53}$$

then, the lifetime $\Gamma_i(\mathbf{k_i})$ due to all the scattering mechanisms included in the simulation is,

$$\Gamma_i(\mathbf{k_i}) = \sum_f (\Gamma^{LO}{}_{if}(\mathbf{k_i}) + \Gamma^{ADP}{}_{if}(\mathbf{k_i}) + \Gamma^{IR}{}_{i.f}(\mathbf{k_i}) + \Gamma^{AD}{}_{if}(\mathbf{k_i})). \tag{2.54}$$

The probability $P(t)$ of an electron scattering in a time interval dt after a free flight time t may be written as the joint probability,

$$P(t)dt = \Gamma_i(\mathbf{k_i}(t)) \exp\left[-\int_0^t \Gamma_i(\mathbf{k_i}(t'))dt'\right] dt. \tag{2.55}$$

The desired random free flight times t_f may be generated according to the probability density $P(t)$ using a uniform pseudo-random number $r \in [0, 1]$.

$$r = \int_0^{t_f} P(t)dt \tag{2.56}$$

Thus,

$$r = 1 - \exp\left[-\int_0^{t_f} \Gamma_i(\mathbf{k_i}(t'))dt'\right]. \tag{2.57}$$

As $1-r$ is statistically the same as r and is also a uniform random number $(1-r) \in [0,1]$, we finally arrive at the fundamental equation for generating free flight times,

$$-\ln(r) = \int_0^{t_f} \Gamma_i(\mathbf{k_i}(t'))dt'. \tag{2.58}$$

In a QCL, the electric field is applied only in the z direction and not in the plane. Therefore, the in-plane momentum in the above equation $\mathbf{k_i}$ is constant during the free flight and the time dependence can be removed yielding the following analytical equation for generating free flight times,

$$t_f = \frac{-\ln(r)}{\Gamma_i(\mathbf{k_i})}. \tag{2.59}$$

Such a simplification cannot be made if the in-plane momentum is a time varying quantity which would be the case for semiconductor devices such as a Gunn diode or a MOSFET. An elegant technique called the self-scattering method can be employed to simplify the free flight integral in such situations [22].

2.8.2 Instantaneous scattering update

All that remains now is to identify the scattering mechanism responsible for removing the electron from it's initial state and the based upon the type of scattering mechanism update the electron's subband and in-plane momentum to a final state addressed by $(E_f, \mathbf{k_f})$. This final state would be the initial state of the electron for the next iteration. To do this, let us return to,

$$\Gamma_i(\mathbf{k_i}) = \sum_f (\Gamma^{LO}{}_{if}(\mathbf{k_i}) + \Gamma^{ADP}{}_{if}(\mathbf{k_i}) + \Gamma^{IR}{}_{if}(\mathbf{k_i}) + \Gamma^{AD}{}_{if}(\mathbf{k_i})).$$

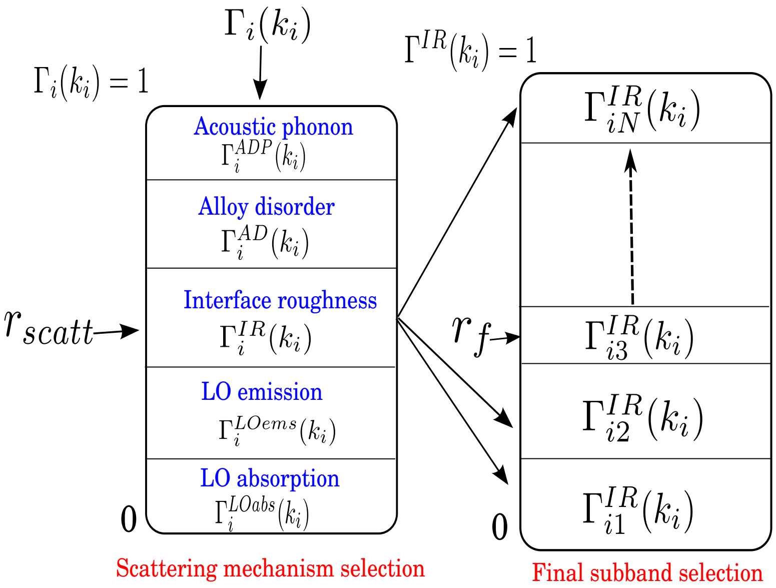

Figure 2.6: Selection of scattering mechanism and final subband.

The same idea which was used to generate free flight times based on the lifetime of the electron can be also be used here with a minor difference that the above equation is a discrete sum and not a continuous integral. By generating two more uniform random numbers $r_f \in [0,1]$ and $r_{scatt} \in [0,1]$ one can probabilistically select the final subband and scattering mechanism. Once the final state f and scattering mechanism have been selected, one can update the electron's subband and in-plane momentum by conserving the total energy and in-plane momentum. This process is schematically illustrated in Fig. 2.6 for an example when interface roughness scattering (IR) is selected.

If E_f denotes the energy of the final subband selected and ΔE_{scatt} the energy exchange during a particular scattering process then,

$$E_i + \frac{\hbar^2 {k_i}^2}{2m^*} + \Delta E_{scatt} = E_f + \frac{\hbar^2 {k_f}^2}{2m^*}. \tag{2.60}$$

The energy exchange for an elastic and inelastic scattering process is illustrated in Fig. 2.7.ΔE_{scatt} for the scattering mechanisms considered in this thesis is tabulated in Table 2.3.

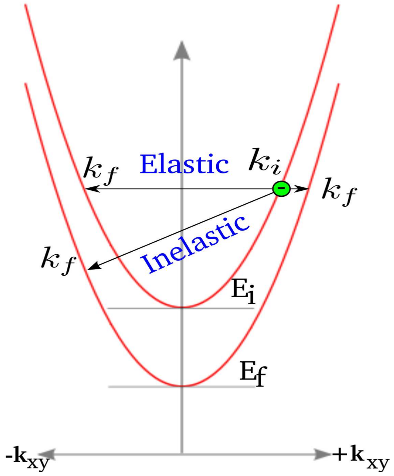

Figure 2.7: Energy exchange for elastic and inelastic processes.

Table 2.3: Scattering energy exchange

Scattering	ΔE_{scatt} (eV)
LO phonon emission	$-\hbar\omega_{LO}$
LO phonon absorption	$\hbar\omega_{LO}$
Acoustic deformation phonon	0
Interface roughness	0
Alloy disorder	0

The sequence of free flights and instantaneous scatterings is illustrated in Fig. 2.8. A time step dt is chosen such that the correct electron dynamics are captured. In each time step all the simulated electrons are allowed to scatter till they cross the time step. Once all the electrons have been followed, one can statistically average physically relevant quantities of the ensemble such as the single particle distribution function and current . It is important to understand that while estimating these quantities, each simulated electron actually represents a sample of the doping and is not a single electron in reality. The simulated electrons are also referred to as particles to avoid this ambiguity.

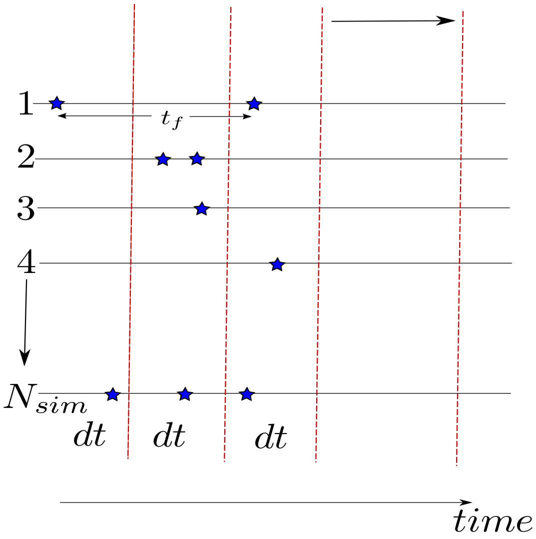

Figure 2.8: Ensemble Monte Carlo method illustration. The blue stars represent instantaneous scattering events and the time between successive scatterings is the free flight time. The vertical red lines represent the time steps at which ensemble averages are calculated to check for convergence to a steady state.

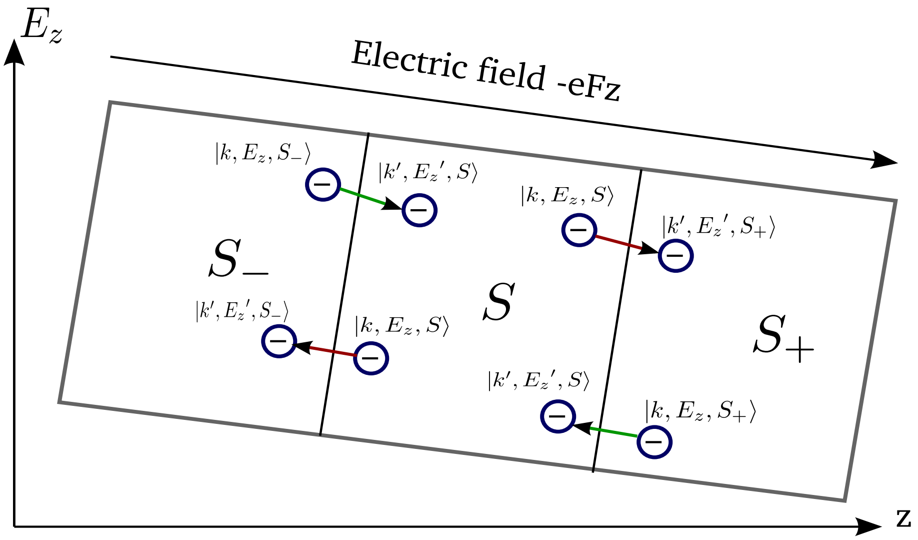

Figure 2.9: Periodic boundary conditions in QCLs for charge conservation.

2.8.3 Periodic boundary conditions

As mentioned before , a QCL contains of a number of stages or periods and the electrons are provided by doping a few layers in each stage. Considering the fact that all the stages are identical it is a reasonable approximation to assume that charge transport should also be the same in all stages. Therefore, one can simulate a generic central stage S bounded by two neighbouring stages S_- and S_+ in order to study transport. Every simulated electron which exits S is properly injected into the corresponding state to ensure charge conservation. These periodic boundary conditions are schematically illustrated in Fig.. Every time a simulated electron in a state $|k, E_z, S\rangle$ makes a transition (represented by red arrows) to a state $k'E_z{}', S_\pm\rangle$, it is properly reinjected into S by the transitions represented by the green arrows. It is sufficient to simulate three stages as the envelope wavefunctions $\psi(z)$ in a stage do not extend beyond their respective neighbouring stages. Every electron that makes an interstage transition carries with it a charge $\pm e$ (+ if $S \rightarrow S_+$ and - if $S \rightarrow S_-$) and this in the model is the method used to calculate current. This is illustrated in Fig. 2.9.

2.9 Synopsis of the EMC method

The EMC method can be summarized with the aid of Fig. 2.10. To summarize, the EMC follows an ensemble of electrons in a device. Each electron experiences a sequences of free flight interrupted by scattering events. At each scattering event, the energy and momentum of the electron are updated. At the end of each time step, Poisson's equation can be solved to update the self-consistent potential. This process is continued until a steady state is reached when the observable dynamical quantities converge to their respective steady state values.

2.10 Summary

In this chapter, the EMC simulator used in this thesis for quantitatively describing electron and photon transport for QCLs has been described in detail. The inputs to the EMC simulator are the electronic states and the scattering rates. The equations describing them have been derived and mathematically formulated. Although the EMC is a semiclassical method, it is a computationally efficient and accurate one which is a good compromise of computational speed and physical accuracy . The questions about coherent transport in QCLs is a complex one and the inclusion of scattering in such methods is a highly non-trivial task. The issues dealing with coherent transport have been discussed in [12, 13, 14, 25].

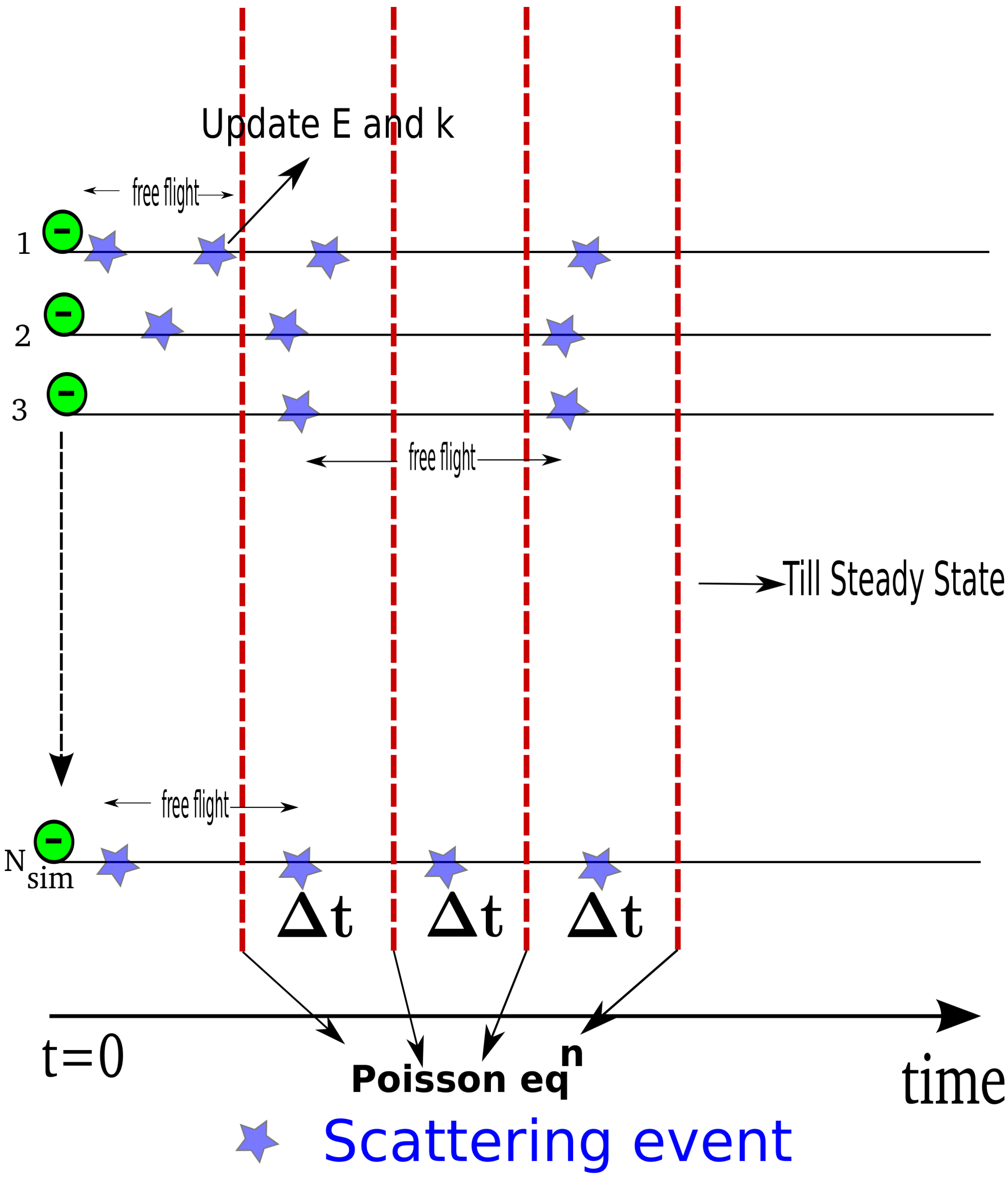

Figure 2.10: Schematic synopsis of Ensemble Monte Carlo method.

Chapter 3

Experimental validation of the EMC method

3.1 Simulation of a voltage pinned QCL

Another good test of the validity of the EMC method is the simulation of voltage clamping in super diagonal QCLs, i.e., QCLs where the upper and lower lasing state are separated very diagonally in space. This has the effect of pinning the electric field in the active region to its threshold value thereby preventing Stark tuning of the lasing transition [41]. Stark tuning is the change in the emission wavelength due to a change in the applied electric field.

This effect can only be captured accurately if the optical cavity dynamics are included correctly and in order to verify this an experimentally fabricated and tested, super diagonal QCL was simulated Fig. 3.1. The upper (u) and lower state (l) have been marked in red to identify the lasing transition.

This device was simulated using the EMC method and as can be seen from Fig. 3.2, the EMC simulator is able to correctly capture the voltage pinning or clamping effect and also gives a quantitative agreement with the experimentally measured I-V curve (top most I-V curve in experimental I-V characteristic). As can be seen from Fig. 3.2, the voltage is pinned to 9V and this effect is captured by the EMC if the optical cavity dynamics are included.

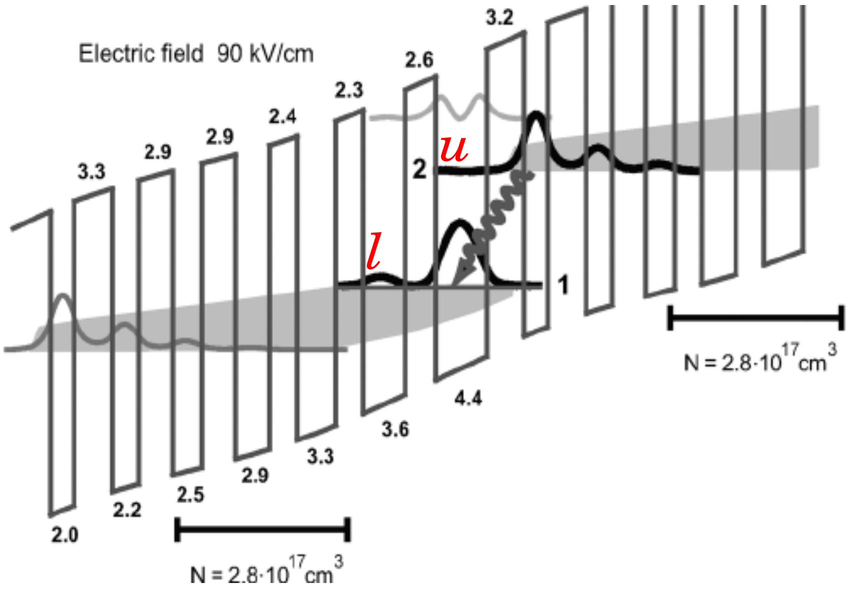

H.Choi et. al, "*Time-resolved investigations of electron transport dynamics based on diagonal lasing transition*", IEEE journal of quantum electronics, 45, 4, 2009

Figure 3.1: A super diagonal QCL used to study voltage pinning.

Experimental I-V

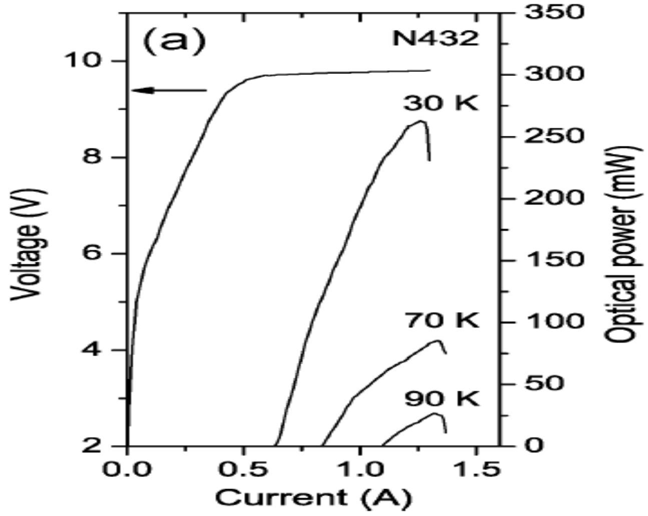

EMC <->Optical Cavity dynamics simulation

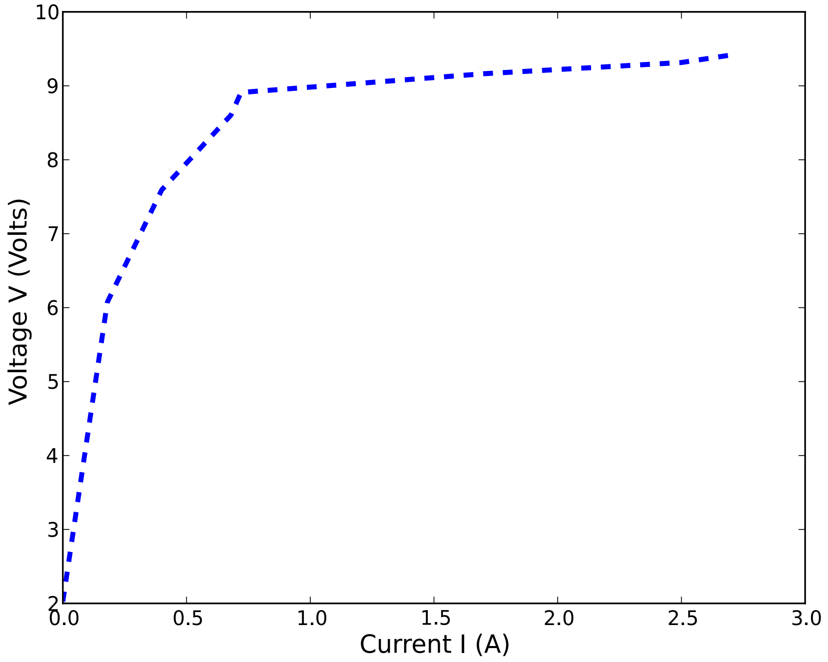

Figure 3.2: Experimentally measured (top) vs EMC simulated (bottom) I-V characteristic of the QCL in Fig. 3.1.

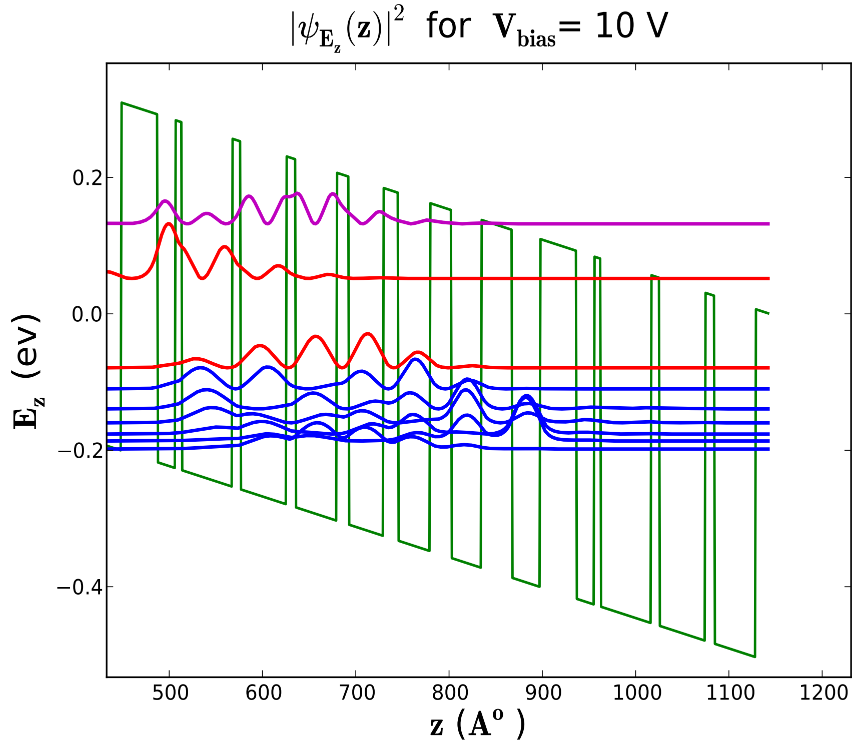

Figure 3.3: Simulated wavefunctions for QCL structure taken from [7].

3.2 Simulation of an electrically tunable QCL

In order to validate the EMC model, a fabricated and experimentally tested QCL from [7] was simulated. The wavefunctions for this QCL were solved using the non-parabolic TISE and they are plotted at a bias of 10 V in Fig. 3.3.

The I-V curve generated using the EMC simulator is now compared to the experimentally measured one from [7] and as can be seen in Fig. 3.4, there is a quantitative agreement between the model and experiment.

As can be seen from Fig. 3.4, the inclusion of the optical cavity dynamics is important to model the QCL accurately. There is an under-estimation of the current density if the photon induced scattering is not included. The

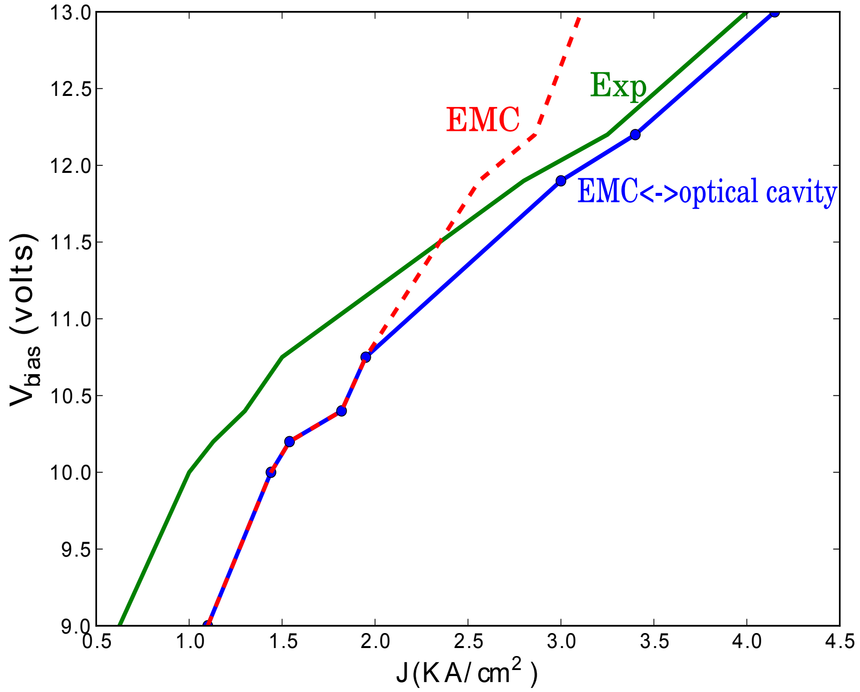

Figure 3.4: EMC simulated I-V curve compared to experimentally measured one for QCL in [7].

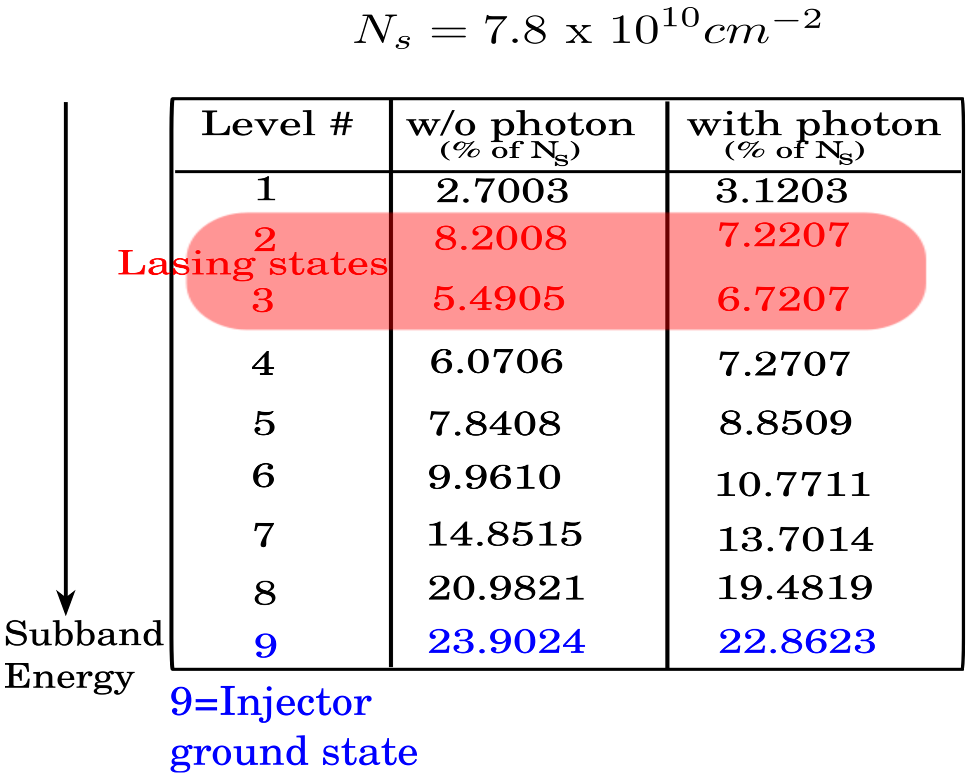

$$N_s = 7.8 \text{ x } 10^{10} cm^{-2}$$

Level #	w/o photon (% of N_S)	with photon (% of N_S)
1	2.7003	3.1203
2	8.2008	7.2207
3	5.4905	6.7207
4	6.0706	7.2707
5	7.8408	8.8509
6	9.9610	10.7711
7	14.8515	13.7014
8	20.9821	19.4819
9	23.9024	22.8623

Figure 3.5: EMC simulated subband populations for QCL in [7].

photon induced scattering between the upper and lower states of the QCL increases the current by decreasing the subband population of the upper state and increasing the population of the lower state. The subband populations of the various states of the QCL are detailed in Fig. 3.5.

The time evolution of the optical mode intensity I_m is plotted in Fig. 3.6 and as can be seen from Fig. 3.6, I_m reaches a steady state value once the gain equals loss condition has been met.

3.3 Summary

The EMC simulation model was validated by simulating two fabricated and experimentally tested QCLs and the simulation results were in quantitative

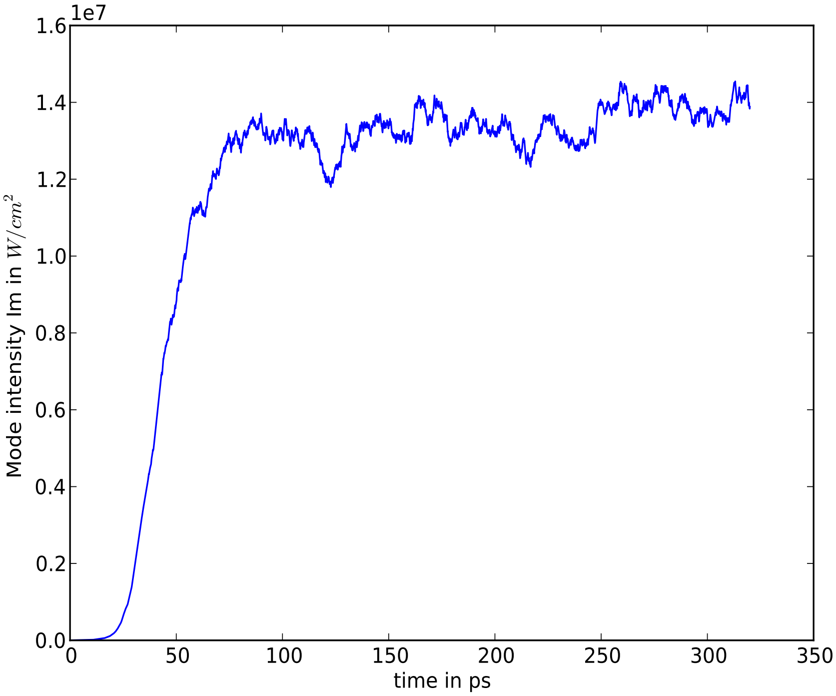

Figure 3.6: EMC simulated time evolution of mode intensity I_m of QCL in [7].

agreement with experimentally measured ones. The inclusion of the optical cavity dynamics was shown to be important for an accurate description of the QCL. Further validation of the EMC model will be given in the next few chapters.

The EMC simulator will be employed in subsequent chapters to simulate proposed novel devices and the results of the EMC simulator which are microscopic quantities will be discussed in detail. Such microscopic quantities are extremely difficult to probe and measure experimentally and they offer great insights into a device's operation and consequently can be used to optimize and improve device performances.

Chapter 4

Injectorless Mid Infrared Quantum Cascade Laser

4.1 Motivation

Since their first demonstration [27], mid infrared (MIR) quantum cascade lasers (QCLs) have been developed to operate at high temperatures and produce high output powers for a wide range of wavelengths from as short as 4 μm to as long as 12 μm [28]. QCLs are attractive sources for applications such as gas and chemical detection, military applications and free-space optical communications to name a few [28, 29]. In particular, QCLs have been trageting two specific wavelength windows of 3-5 μm and 8-12 μm for communication purposes and also because the fundamental vibration modes of many trace gases and molecules fall in these wavelength ranges [28, 29].

The operation of most existing MIR QCLs relies on the injector regions which are alternated with the active regions and perform several important functions such as transport and injection of electrons from one active region to the next, convenient space for doping, isolation of the upper laser state from the continuum thereby reducing parasitic leakage currents and "cooling" of the electron gas. However, the presence of the injector region has some significant drawbacks namely the lengthening of the QCL period which can result in an additional voltage drop across the injector, restriction on the number of QCL periods due to the long period length and longer transport times due to scattering in the injector region which limits the dynamic range of operating current. The additional voltage drop in the injector reduces the wall-plug efficiency (WPE) as a majority of the applied voltage is not used for producing photons. Recently, injectorless quantum cascade lasers have been proposed to overcome the aforementioned drawbacks. A comprehensive review and analysis of the injector regions in a QCL can be found in [29].

The salient features of injectorless or short injector QCLs have been the use of highly strained material systems to increase the band offset in order to ensure isolation of the upper state from the continuum, short period lengths which allow for a larger number of periods compared to injector based QCLs , shorter transport times, low voltage defect, resonant phonon depopulation of the lower state and resonant tunneling (RT) as the injection mechanism. Their low temperature performance has exceeded the performance of injectorbased MIR QCLs and WPEs exceeding 50 %, several watts of output power and low threshold current densities have been demonstrated at the shorter end (4-6 μm) of the MIR spectrum [31, 30]. However, due to a combination of thermally activated phonon scattering, parasitic X valley leakage and thermal backfilling, their high temperature performance has shown drastic degradation and they also suffer from low characteristic temperatures (T_0) in the range of 120 to 125 K. Such low temperatures would indicate the need for drastic cooling of the QCLs. Due to the shorter period length, higher operating electric fields and voltages are required which is also undesirable due to carrier heating. Some of the issues such as the parasitic X valley leakage and thermal backfilling have been addressed by the use of multiple alloy heterostructures with variable barrier heights to prevent leakage and double and triple resonant LO phonon depopulation schemes to decrease thermal backfilling [32] . These designs would involve complications due to the presence of the multiple alloys. Another important issue is the lack of an energetic barrier that a long injector QCL would offer. This barrier prevents parasitic current from the active region of one period to the injector of the previous period. The absence of such a barrier has greatly impaired the high temperature performances of short injector QCLs [33]. Also, most of the injectorless QCLs cited in this section have focused on emitting at shorter wavelengths due to the fact that the optical losses increase approximately as the square of the wavelength [36]. Hence, due to the increased optical losses, it is always more challenging to design QCLs at the longer end of the MIR spectrum.

In this chapter, a conceptually simple long wavelength injectorless QCL emitting in the range of 11-12 μm is proposed utilizing scattering assisted (SA) injection as opposed to the conventional RT injection scheme and whose operating electric field is significantly lower in comparison to the best performing injectorless QCLs. The use of multiple alloys has been avoided and it is has also been ensured that parasitic leakages into the neighboring periods' injector regions have been minimized by appropriate wavefunction engineering. The benefits of the SA injection scheme have been realized both in very long injector MIR and the terahertz QCLs [37, 38]. Detailed comparisons between SA and RT injection QCLs with thorough analysis have been presented in [37, 38]. In the following sections, the design and concept of the proposed structure will be described. The simulation model will be briefly described and validated against published experimental data. The model will be used to investigate the performance of the proposed structure and the simulation results will be used to highlight the advantages of the design when compared to existing injectorless QCLs.

4.2 Proposed Design

A $In_{0.6}Ga_{0.4}As/In_{0.44}Al_{0.56}As$ SA injection QCL grown on an InP substrate is proposed. The same material system as the one used in [40] is employed. This material system provides a large conduction band offset of 663 meV thus preventing carrier leakage into the continuum and also a lighter effective mass of $m^* = 0.040216m_0$ (when compared to the matched InP/InGaAs/InAlAs system) in the well layers which facilitates electron transport. The layer thicknesses of one period of the QCL in A°, starting from the injection barrier are **40**/40/**23**/32/**12**/68/**13**/54/**28**/48 with the bold and regular numbers representing $In_{0.44}Al_{0.56}As$ and $In_{0.6}Ga_{0.4}As$ layers, respectively. The underlined layers have been doped with a volume doping density of 8.37×10^{16} cm^{-3} corresponding to an approximate sheet charge density of n_s=6.36 $\times$ 10^{10} cm^{-2} identical to the doping levels in [40]. The electronic states of the QCL are plotted in Fig. 4.1. The energy levels and wavefunctions described by the nonparabolic Schrödinger equation have been computed by employing a finite difference solver [42]. A rather thick injection barrier has been used to isolate the upper state from the injector. The length of this device is 362 A° and even though this is slightly longer than previous injectorless QCLs, its performance in subsequent sections of this chapter will be shown to more than compensate for the slight increase in device length. However, the

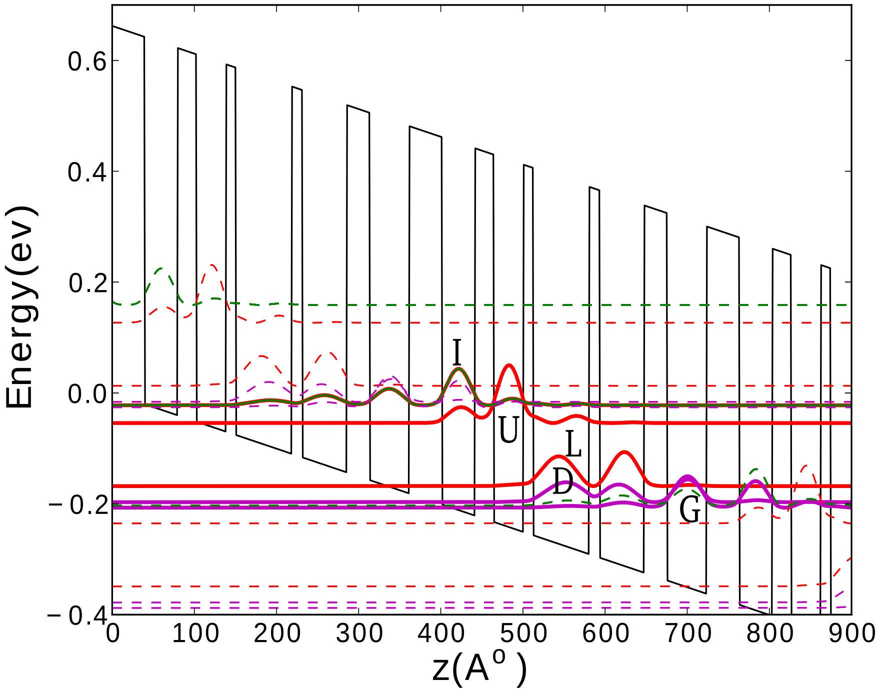

Figure 4.1: Conduction band profile and probability densities of the proposed QCL for an applied electric field of 50 kV/cm. The central period's states are plotted with solid lines and the neighboring periods' states are the dashed blue lines. The upper and lower states are separated by 113.8 meV which corresponds to a lasing wavelength of 10.9 μm.

proposed device is still much shorter than most conventional injector based QCLs. The QCL has also been designed to have a slight larger optical dipole matrix element when compared to a previous design [40] in order to enhance the optical gain.

Each period of the proposed QCL has five states. The upper (U), lower (L), depopulation (D) and intermediate (I) states have been marked in the figure along with the ground state (G) of the QCL. The lasing transition is diagonal which ensures a long upper state lifetime. The state D acts as a depopulation state for the lower lasing state and is approximately one LO phonon energy below it which ensures fast depopulation. The highly diagonal lasing transition coupled with the fast LO phonon assisted depopulation greatly improves the temperature performance of a QCL and it's advantages have been demonstrated both in MIR and THz QCLs. At the peak gain electric field, state G of one period is resonantly aligned with state I of the next period. G injects carriers into I of the next period which subsequently injects carriers into U via LO phonon scattering. States U and I are separated by one LO phonon energy which ensures that the U state holds a majority of the carriers and the population of I is kept small. This is one of the main advantages of the SA injection mechanism over the RT injection mechanism. In RT injection QCLs, state U directly aligns with G and can typically hold at most half the sheet charge density $n_s/2$ thus limiting the optical gain. The SA injection scheme circumvents this limitation and the U state can hold a majority of the electrons thereby enhancing the gain [37, 38]. This would also imply that the population of state G is also kept low which minimizes thermally activated backfilling of state L which is one of the major reasons for temperature related performance degradation of QCLs. Also, isolation of U from state G of the previous period reduces parasitic scattering mechanisms which will be detailed in the following sections. This would not have been possible in a RT QCL where G and U are aligned.

4.3 Method and Validation

A ensemble Monte Carlo (EMC) simulator has been developed to study electron transport in QCLs. This will be used in subsequent sections to analyze the performance of one the best performing long wavelength short injector design and also to compare it with the performance of the proposed QCL. The optical cavity field has also been included and both the electronic and optical features of a QCL can be modeled [43] . The spectral gain based on lifetime broadening is used in this model and has been shown to agree reasonably with experiment [44]. The electron scattering mechanisms included in the simulation include LO and acoustic phonon, interface roughness and alloy disorder scattering. The bulk phonon approximation is adopted [45] and a LO phonon energy of approximately 31 meV has been calculated based on the mole fraction weighted average of the phonon energies of InAs and GaAs. The contribution of AlAs-like branch to the phonon energy has been neglected as it is not too important [45]. Interface roughness scattering is usually characterized by a mean height Δ and correlation length Λ. Experimental studies suggest a product of $\Delta\Lambda \approx 1$ nm^2 for the InGaAs/InAlAs material system and and therefore $\Delta = 0.06$ nm [45] has been fixed. Due to the high indium content in InGaAs, random alloy scattering has been included with a scattering potential of 0.3 eV [45]. Space charge induced corrections to the conduction band potential for MIR QCLs have been shown to be negligible [46] and therefore have not been considered along with electron-electron and electron-impurity scattering. In [46], EMC simulations revealed that electron-electron scatterings contributed less than 4 % to the device current. EMC simulations of another short injector MIR QCL [47] based on a similar material system have also revealed that Coulomb interactions, i.e., electron-electron and electron-impurity scattering practically do not contribute to the current and have also been shown to have only a moderate influence on the optical gain of the device. Also, the sheet charge doping levels of the QCLs simulated in this paper are of the order of 10^{10} cm^{-2} which is quite low even for MIR QCLs and it has been shown that electron-electron scattering in particular is more effective at higher densities [48]. In order to reduce the computational load and due to the aforementioned reasons, it is a reasonable approximation to neglect Coulomb interactions in the EMC simulation of the MIR QCLs simulated in this paper.

In order to validate the method, the EMC simulator is used to calculate the temperature dependent current densities of two experimentally realized injectorless RT QCLs operating at 5 μm [39] and 9-11 μm [40] (depending on the operating temperature). A total optical loss and confinement factor of a_{tot}= 4.18 cm $^{-1}$ and $\Gamma = 0.62$ for the short wavelength device [39] were assumed. Only a confinement factor of Γ= 0.36 was given for the long wavelength device in [40] and the optical loss was not mentioned. Hence, a_{tot}=14.4 cm $^{-1}$ which is typical for longer wavelength MIR QCLs [36] has been assumed.

The characteristic temperature T_0 which is a measure of the increase in the threshold current density as the operating temperature increases is a key device metric and a higher T_0 is always desirable. The current densities usually increase exponentially with temperature. The characteristic temperatures for the above mentioned devices are 114 K and 173 K respectively which are substantially lower than the typical T_0 of a conventional

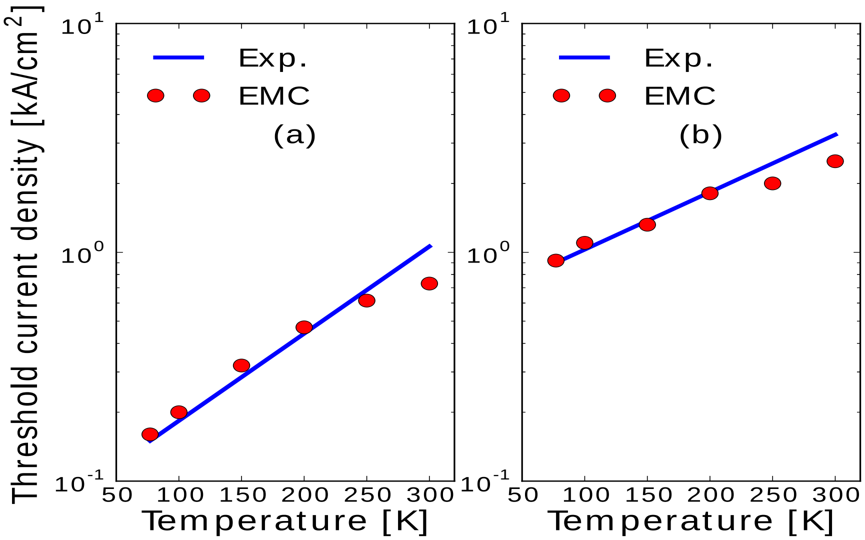

Figure 4.2: Comparison between experimental (blue solid lines) and EMC generated(red circles) temperature dependent current density of two short injector MIR QCLs. (a) is a 6 μm QCL experimentally demonstrated in [39] and (b) is a 9-11 μm QCL which was demonstrated in [40].

long injector QCL. In Fig. 4.2, the threshold current densities (plotted on a logarithmic scale in order to generate linear curves) for various operating temperatures calculated using the EMC simulator are compared with the experimentally determined current densities of the the short wavelength QCL [39] in Fig. 4.2(a) and the long wavelength one [40] in Fig. 4.2(b). The EMC simulations agree quantitatively with the experimental curves. The simulations slightly underestimate the threshold current densities above 200 K as can be seen in Fig. 4.2. The reason for this discrepancy is that a temperature independent optical loss has been assumed for all devices in this chapter as is commonly done in the EMC [45]. This is however a rather simplistic approximation and it has been shown that the temperature dependence of the optical loss is highly non-trivial [49] and depends on many factors including the transport in the active region of the QCL. Also, the Drude model approach adopted in [36] is a rather simplistic approach and is inaccurate. The temperature dependence in the Drude model is solely reflected in the temperature dependence of the bulk mobility of the active region. This is a rather gross simplification since the active region in a QCL is a superlattice and not a bulk material. It is beyond the scope of this thesis to deal with the temperature dependence of the optical losses as the temperature induced change in the losses is still an active topic of research.

In the next section, the proposed QCL will be simulated and its results will be compared with the results of the long wavelength injectorless QCL [40] mentioned in this section. This device which will be referred to as the reference device is one of the best performing injectorless QCL in the long MIR. Both the proposed and reference device have identical doping which would make for a fair comparison of their performances.

4.4 Simulation results

Since the proposed QCL operates in a similar wavelength range to the reference device [40], it is reasonable to assume that the proposed device will also have the same loss and optical confinement factor as the reference design. This results in an effective loss of $a_{eff} = a_{tot}/\Gamma$= 40 cm^{-1}. This assumption is accurate as a first approximation and for a more accurate estimation of the waveguide losses and optical confinement factor, a thorough modeling of the waveguide region needs to be carried out which is beyond the scope of this thesis and a suggested method for doing this is given in [36]. The operating electric field range of the proposed device is from 43 to 50 kV/cm depending on the temperature. This changes the emission wavelength from about 11 μm to 12 μm as the temperature increases from 77 K to 300 K. The peak (unsaturated) [43] gain for the proposed and reference device has been plotted in Fig. 4.3 for temperatures varying from 77 K to 300 K. The temperature independent effective loss which is the same for both devices is also plotted in the same figure. As can be observed, the proposed device has nearly double the optical gain of the reference device at 77 K and has higher gain than the reference device at all temperatures. This is a good indication that the proposed design could potentially have higher operating temperatures than the reference design. The reason for the increased gain is due to the SA assisted injection scheme and can be explained by looking at the transport times across the injection barrier for both the reference and proposed design. In Fig. 4.4 and Fig. 4.5, the energy resolved electron densities for the reference and proposed design are shown respectively. For the reference design in Fig. 4.4, one can see that the upper and ground states hold most of the electrons and that the electrons are evenly distributed between the two states. In Fig. 4.5, the SA injection scheme of the proposed design facilitates for a much larger number of electrons to reside in the upper state while also depleting the ground state.

Referring to Fig.4.1, τ_f defines the transport time for an electron to scatter from states L, D and G of one period to U and I of the next period and by τ_b the reverse process. It is straightforward to calculate scattering times in the EMC by averaging over all the possible k-states and the procedure to do so has been detailed in [44]. These two transport mechanisms are essentially the scattering processes that contribute to the current of the QCL. τ_f is a measure of how fast the electrons scatter across the injection barrier while τ_b represents parasitic scattering which scatters carriers away from the upper state and to the injector states in the preceding period. Such scattering processes are undesirable and they reduce the optical gain. It is evident that their ratio τ_b/τ_f must be as large as possible in order to efficiently transport electrons into the active region of the QCL thereby maximizing the gain. In Fig. 4.6, this ratio is plotted as a function of temperature and the proposed design maintains a higher τ_b/τ_f ratio over all temperatures. The reason for this is that in the SA injection scheme the upper state is spatially and energetically separated from the ground state of the previous period

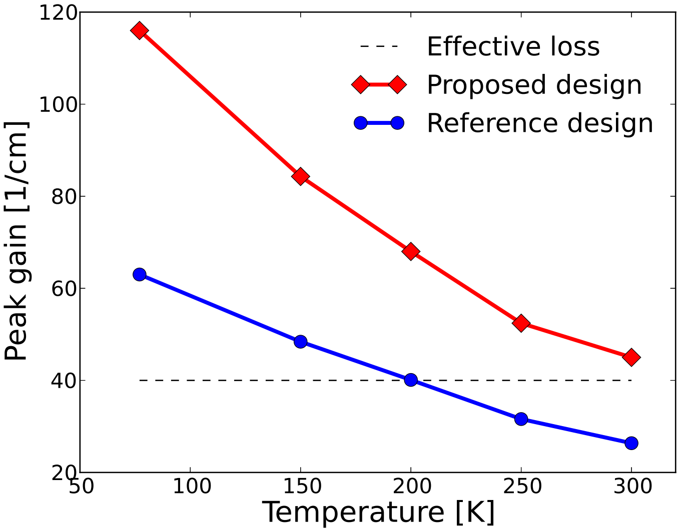

Figure 4.3: Peak gain as a function of temperature for the proposed and reference designs. The dashed black line indicates the temperature independent effective loss. In the simulation of the reference design, we have limited the maximum applied electric field to a value which corresponds to the resonant alignment of the ground state and upper state. The reasons for this are explained in more detail in the text.

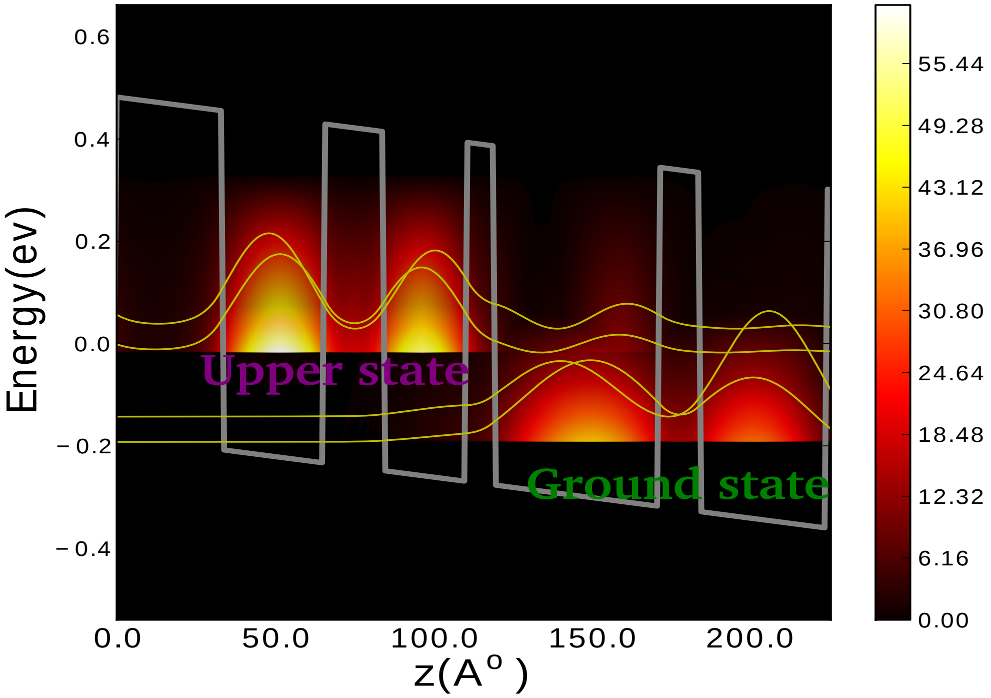

Figure 4.4: Energy resolved electron density for reference device at 77 K at peak operating electric field. The corresponding probability densities of the QCL states have also been plotted using solid yellow lines to illustrate the spatial variation of the wavefunctions of the QCL states.

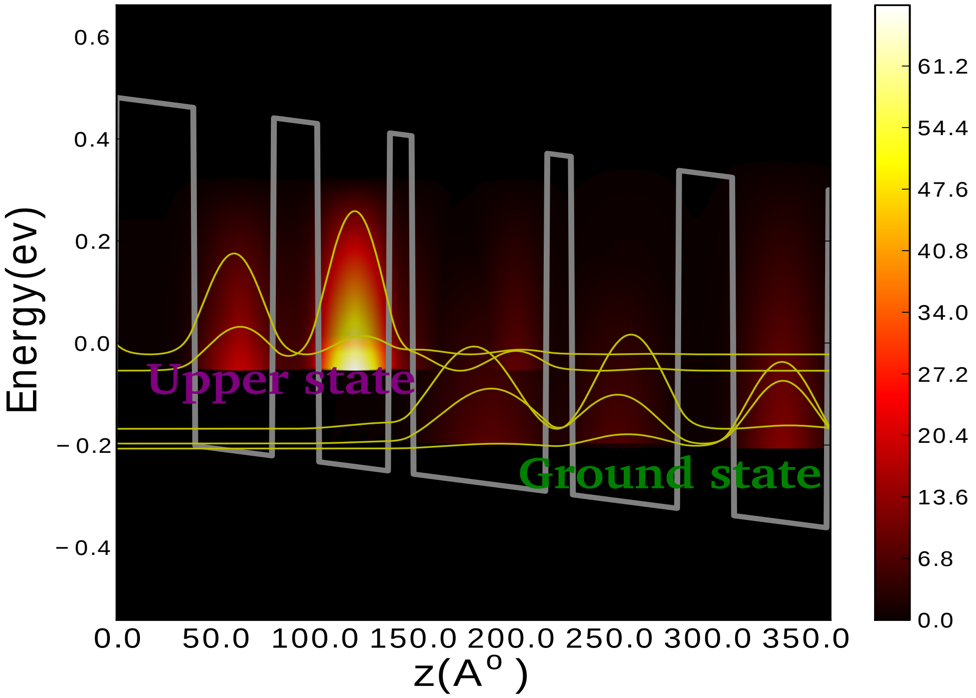

Figure 4.5: Energy resolved electron density for proposed device at 77 K at peak operating electric field. Similar to Fig. 4.4, the probability densities of the QCL states have also been plotted.

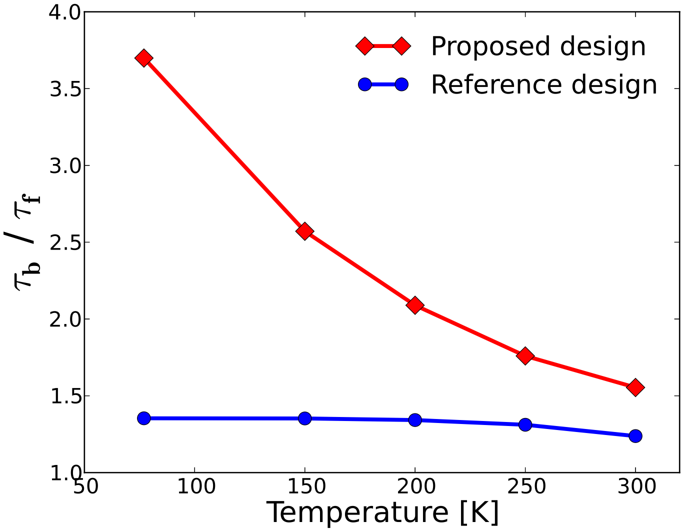

Figure 4.6: Ratio of backward to forward electron transport times τ_b/τ_f (dimensionless quantity) as a function of temperature for the proposed and reference designs.

which greatly reduces scattering out of the upper state thereby increasing its population and subsequently the optical gain.

For the simulation of the reference device in this section, the maximum applied electric field has been limited to a value which corresponds to the resonant alignment of the ground state and upper state which is the intended peak operating point for a RT QCL. However in [40], the authors have pointed out that such a field is not sufficient to overcome the losses and that an additional 30 kV/cm electric field would be required. This fact is also observed in Fig. 4.3 where it is clear that the reference device cannot overcome the losses above 200 K. Such a large incremental electric field meant that the reference device began to function unintentionally as a SA injection QCL with a key difference that the intermediate state was not one LO phonon energy above the upper state. This mode of operation would increase the gain of the reference device to levels comparable to the proposed design. However, the reference design will be less efficient as the 30 kV/cm increment in the electric field would result in a 4 V increase in the operating voltage. In addition, the current would increase by about 1.4 times and as a result the input electrical power would be about twice that of the reference design. This would clearly result in heating and degradation of the gain. Incorporating heating effects self-consistently with the electron transport [50] model is a challenging task and such a model is beyond the scope of this thesis and would require extensive computational time in order to be accurate.

The temperature dependent threshold current density of the proposed device is plotted in Fig. 4.7. The curve can be approximated accurately by the usual exponential fit with a characteristic temperature of T_0=260 K which is much higher than the typical characteristic temperatures of injectorless QCLs and is even comparable to the characteristic temperatures of conventional injector based QCLs. The threshold current density at 77 K is found to be 0.85 kA/cm^2 which is extremely low for QCLs in this wavelength range and is comparable to the values of many conventional long injector MIR QCLs. The high temperature threshold current density is 1.95 kA/cm^2 which is also extremely low.

The wall-plug efficiency η_{wp} is an important metric of a QCL's performance. It is given by the ratio of the optical power P to the input electrical power (product of applied voltage V and electrical current I) and by adopting a simple rate equation approach [29], one can show that it can be approximated by,

$$\eta_{wp} = \frac{J_{max} - J_{th}}{J_{max} V} \frac{dP}{dI}. \tag{4.1}$$

Here, J_{max} is the current density at the maximum operating field and V the applied voltage at the same field. Modeling the optical power of a QCL would require information about quantities such as the collection efficiency [43] and other parameters of the waveguide which can be hard to model quantitatively. However, one can further simplify η_{wp} by observing that the optical power would be proportional to the optical gain $P \propto g$ and by noting that the current and current density are proportional to each other, a measure of the wall-plug efficiency can be defined. We denote this measure (which is proportional to η_{wp}) by $\tilde{\eta}_{wp}$ and it is given by,

$$\eta_{wp} \propto \tilde{\eta}_{wp} = \frac{J_{max} - J_{th}}{J_{max} V_p} \frac{dg}{dJ}. \tag{4.2}$$

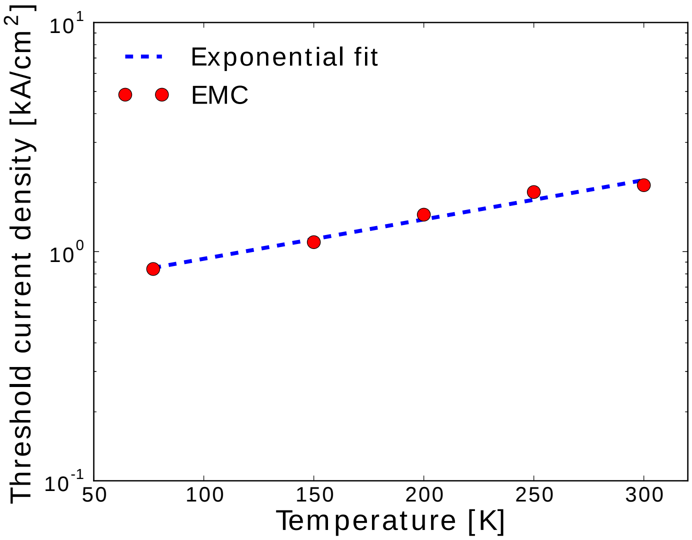

Figure 4.7: EMC generated (red circles) temperature dependent current density (J_{th}) of the proposed QCL for temperatures ranging from 77 K to 300 K. The dashed blue line is an exponential fit described by $J_{th}(T) = J_0 \exp(T/T_0)$ with J_0=0.85 kA/cm^2 and T_0= 260 K.

Table 4.1: Wall-plug efficiency parameters for reference and proposed design at 77 K.

Parameter	Reference design 77K	Proposed design 77 K
J_{th}[kA/cm^2]	0.95	0.85
J_{max}[kA/cm^2]	1.5	1.8
dg/dJ[cm/kA]	40	80
V_p[V]	0.18	0.181
$\tilde{\eta}_{wp}$[cm/(V-kA)]	81	233.27

V has been replaced by the voltage drop per period V_p so as to eliminate the dependence on the number of periods. In Table 4.1, $\tilde{\eta}_{wp}$ has been compared for both the reference and proposed design at 77 K. Since the reference and proposed design have the same optical losses and sheet charge densities, the much larger $\tilde{\eta}_{wp}$ of the proposed design should imply that the proposed design would a have a much larger wall-plug efficiency η_{wp} than the reference design.

Although the proposed design has exceeded the performance of the reference design in many aspects, there are a few areas in which the proposed device's performance can be optimized. As can be seen from Fig. 4.3, the peak gain of the proposed device decreases with increasing temperature similar to the reference design. The reasons for this are the increased phonon absorption from the upper to the intermediate state and also due to the more vertical nature of the lasing transition of the proposed design which is a result of the increased optical dipole matrix element of the proposed design. The phonon absorption to the intermediate state could be decreased by varying the energy spacing and the overlap between the intermediate and upper states. Decreasing the optical dipole matrix element would imply a more diagonal QCL and it's advantages and disadvantages have been studied in [51]. This could potentially stabilize the optical gain against increasing temperatures at the cost of a lower optical gain due to the decreased overlap between the lasing states.

4.5 Summary

In this chapter an injectorless, long wavelength MIR QCL emitting in the wavelength range of 11-12 μm has been proposed targeting the 8-12 μm wavelength window where QCLs can be used for multiple applications. An EMC simulator was developed to study transport in QCLs and it was validated against published experimental data by simulating two existing injectorless designs. Using the EMC simulator, the proposed device is shown to have almost double the optical gain compared to one of the best performing long wavelength injectorless QCL and the reason for this has been shown to be the improved transport across the injection barrier minimizing scattering away from the upper state. This was achieved using a scattering assisted injection scheme as opposed to the conventional resonant tunneling injection. The device simulation yielded low threshold current densities of 0.85 k/cm^2 and 1.95 k/cm^2 at 77 K and 300 K respectively. The proposed design is also expected to have a higher wall-plug efficiency. Further improvements can be achieved by optimizing the scattering assisted injection and diagonalizing of the lasing transition.

Part II

Terahertz Graphene Oscillator

Chapter 5

Graphene based Terahertz Oscillator

5.1 Motivation

The generation and detection of electromagnetic waves in the terahertz (THz) frequency range have been active areas of research. Optical and microwave technologies have been used to attempt to bridge the "THz gap". The gap is illustrated in Fig. 5.1 where the power performances of various electronic and optical sources are compared in the vicinity of this gap. As can be seen from Fig. 5.1, there is a lack of viable and compact fundamental sources in this region and in particular at room temperature. THz radiation in this region displays unique characteristics such as a strong sensitivity to polar liquids, spectroscopic responses to a range of materials and enhanced transmission through a range of plastics [53]. These features can be applied to important applications such as medical diagnostics and imaging, ultra-high-speed communications, remote detection of explosive substances and drugs through spectroscopic response of crystalline compounds and non-destructive imaging of items concealed in packaging to name a few [53, 54].

Gunn diode oscillators employ the negative differential resistance (NDR) of III-V materials such as GaAs, InP and GaN to generate power in the microwave and THz frequency range. NDR in III-V materials is a consequence of the electric field induced transfer of electrons into valleys with higher effective mass. This produces the effect of reducing the velocity with

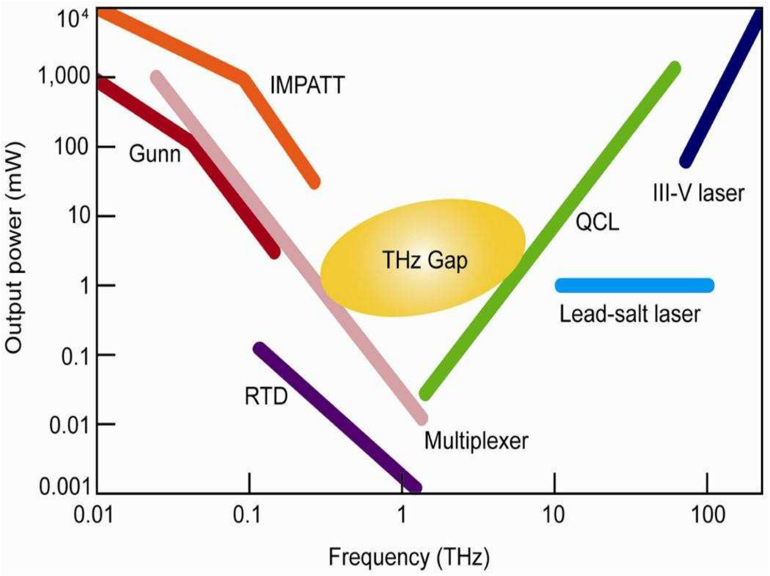

Figure 5.1: Power performance of different sources in the vicinity of the THz gap. Figure taken from [52].

increasing electric fields. These oscillators represent a negative resistance when biased in the NDR and when placed in an appropriate resonant circuit which offer a positive impedance, high frequency oscillations are produced [55]. The frequencies of these devices are limited by the saturation velocities of the materials which are not high enough to reach the frequencies in the THz gap. Another material which exhibits NDR is suspended graphene which is a two dimensional (2D) honeycomb lattice sheet [57, 58]. However, suspended graphene has ultra-high mobility and exhibits velocities which are about 4-5 times higher than the typical saturation velocities of III-V materials. Equally important is the fact the graphene exhibits ultra-high mobility and velocities at room temperature which coupled with the high thermal conductivity of graphene, make it a promising candidate to be a fundamental source of THz radiation at room temperature if oscillations can be achieved. Also, with advances in experimental and fabrication techniques, it is possible to suspend a doped layer of graphene between two electrical contacts [56, 59] thereby opening up avenues for practical device realizations. An example of a recently fabricated and tested suspended graphene set up is illustrated in Fig. 5.2

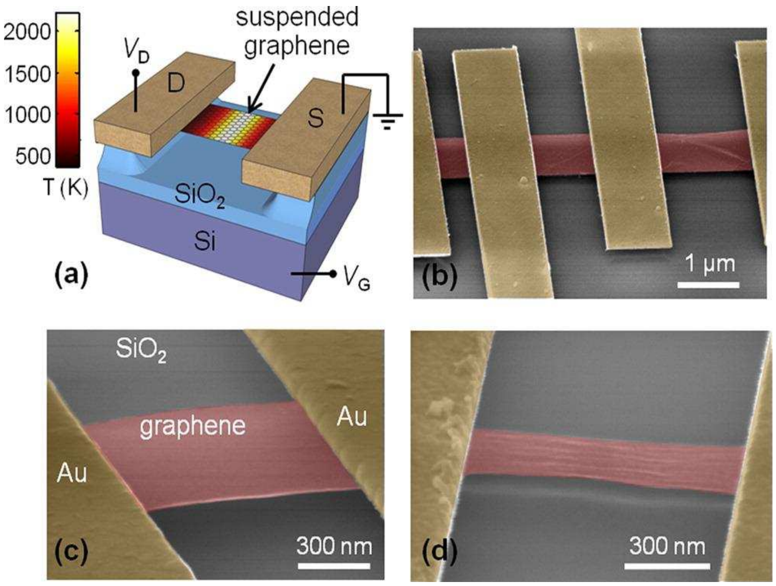

Figure 5.2: Schematic of a suspended graphene device along with SEM images of suspended graphene. Figure taken from [56].

In the next few sections, a novel electronic oscillator based on single layer suspended graphene will be proposed. First, the theoretical aspects of suspended graphene will be elucidated. The device concept will be then be simulated using a self-consistent Ensemble Monte Carlo-Poisson simulator and the results of the simulator will be described in detail. In particular, the microscopic quantities responsible for the oscillations will be illustrated and explained.

5.2 Bandstructure of graphene

Electrons in a single layer of suspended graphene can be described reasonably well for energies in the vicinity of 1 ev by a linear $E-k$ dispersion,

$$E(k) = \hbar k v_F \tag{5.1}$$

where $k = \sqrt{{k_x}^2 + {k_y}^2}$ is the 2D wave vector describing the momentum space of electrons in the (x-y) plane of the graphene sheet and $v_F = 10^6$ m/s is the Fermi velocity. The derivation of this most interesting bandstructure will be given in Appendix C. The semiclassical definition of effective mass m^* for electrons in any semiconductor is usually given by a parabolic dispersion and is,

$$m^*(k) = \hbar^2 \left(\frac{d^2E(k)}{dk^2} \right)^{-1} \tag{5.2}$$

and this definition would clearly result in a diverging effective mass for electrons in graphene. However, an alternate description for the effective mass exists and is given by,

$$m^* = \hbar^2 k \left(\frac{dE(k)}{dk} \right)^{-1}. \tag{5.3}$$

The above equation can be again derived using semiclassical arguments where the momentum of a particle is defined as $p = \hbar k = m^* v_g$ with v_g being the group velocity of a "packet" of electrons and is given by $v_g = \frac{1}{\hbar}\frac{dE(k)}{dk}$.

This definition of the effective mass is consistent with both the parabolic and linear dispersions. Applying the linear dispersion of graphene to this definition of the effective mass yields,

$$m^*(k) = \frac{\hbar k}{v_F}. \tag{5.4}$$

At $k = 0$, the effective mass is zero and this partially appears to justify why electrons in graphene are often called "masless" Dirac fermions. Another distinguishing feature of electrons in graphene is that the effective mass is a function of the wavevector and more importantly is proportional to the wave vector and this implies that the effective mass increases with increasing wave vector within the same energy valley. In III-V semiconductors such as GaAs, InP and GaN, the effective mass of the electrons changes abruptly from a low value in the Γ-valley to a higher value in the L-valley. Electrons are transferred in higher effective mass valleys by a combination of increasing electric fields and phonon scattering. This is the famous Ridley-Watkins-Hilsum theory (RWH) by which NDR is developed in a bulk semiconductor in the presence of an applied voltage [60]. The continuous increase of effective mass in graphene suggests that NDR is also possible in the presence of an applied voltage and phonon scattering. This effect will be studied in the next few sections by first detailing the scattering mechanisms in suspended graphene and then simulating its velocity-field (v-F) curve.

Assuming that the electric field is applied in the y-direction, the velocity in the y-direction can also be calculated using semiclassical arguments. Using semiclassical arguments, the velocity of an electron is given by $v = \frac{\hbar k_y}{m^*(k)}$. Using $m^*(k) = \frac{\hbar k}{v_F}$ yields,

$$v = v_F \frac{k_y}{k}. \tag{5.5}$$

5.3 Scattering mechanisms in graphene

The main scattering mechanisms which govern electron transport in graphene are acoustic and optical phonon scatterings which are modeled using deformation potentials. For the electron densities considered in the subsequent sections, it is a reasonable approximation to neglect degeneracy due to Pauli's exclusion principle and impurity scattering [61, 62].

The intravalley acoustic phonon scattering rate is given by [58],

$$\left(\frac{1}{\tau_{\mathbf{k}}}\right)_{ac} = \left(\frac{k_B}{4\hbar^3 v_F^2 \rho_m v_s^2}\right) D_{ac}^2 T E_{\mathbf{k}}\,, \tag{5.6}$$

where v_s denotes the sound velocity, $\rho_m \approx 7$ x 10^{-8} g/cm^2 is the mass density and $D_{ac} = 6.8$ eV is the acoustic phonon deformation potential. The total optical phonon scattering rate including emission and absorption is given by [58],

$$\left(\frac{1}{\tau_{\mathbf{k}}}\right)_{op} = \frac{D_0^2}{\rho_m \omega_0 (\hbar v_F)^2} \left[\left(E_{\mathbf{k}} - \hbar\omega_0\right)\left(N_{\mathbf{q}} + 1\right)\Theta\left(E_{\mathbf{k}} - \hbar\omega_0\right) + \left(E_{\mathbf{k}} + \hbar\omega_0\right) N_{\mathbf{q}}\right], \tag{5.7}$$

where N_q is the optical phonon occupation number and is governed by Bose-Einstein statistics, $\Theta(x)$ is the Heaviside step function, D_0 is the optical phonon deformation potential and $\hbar\omega_0$ is the optical phonon energy. At the zone edge, there is no distinction between acoustic and optical modes. Hence, intervalley longitudinal acoustic (LA) and transverse acoustic (TA) phonons are modeled as optical phonons with a deformation potential of $D_0 = 3.5$ x 10^8 eV/cm and a phonon energy of $\hbar\omega_0 = 124$ meV. Transverse optical

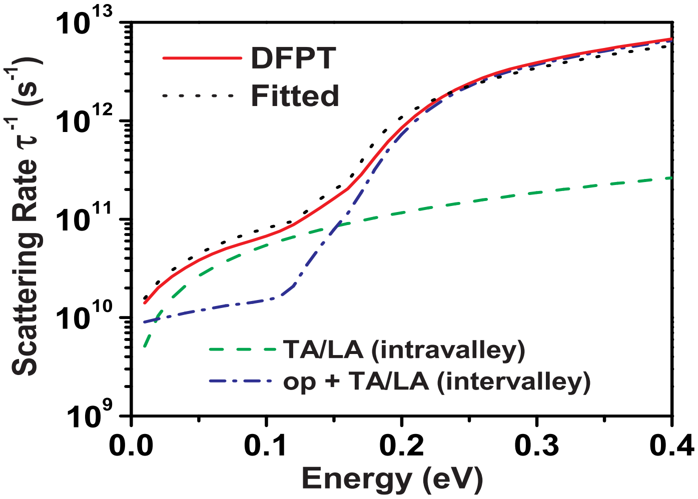

Figure 5.3: Total scattering rate in graphene as a function of the electron energy at 300 K calculated using deformation potentials in comparison with scattering rate calculated using DFPT. Figure taken from [58].

(TO) and longitudinal optical (LO) phonon scatterings are combined and calculated using $D_0 = 10^9$ eV/cm and $\hbar\omega_0 = 164.6$ meV [62, 58].

The total scattering rate is found by adding all the scattering rates due to intravelley acoustic phonon, TA-LA and TO-LO. The total room temperature scattering rate found using the equations in this section compares well with density functional theory (DFT) based *ab initio* scattering rates calculated using DFT and DFPT (QUANTUM-ESPRESSO) [58]. The comparison between the two methods is illustrated in Fig. 5.3.

As can be seen from the form of the scattering rates, the scattering mechanisms in graphene are randomizing which is typical of scattering mechanisms described by deformation potentials. A scattering event for an electron will induce a randomizing of the wave vector. Acoustic phonon scattering in graphene is elastic while optical phonon emission and absorption are inelastic and change the energy of an electron by $\pm\hbar\omega_0$.

5.4 EMC simulator for graphene

In order to model electron transport in graphene, an EMC simulator adapting the EMC simulation framework described previously for QCLs in chapter chapter 2 has been developed. An ensemble of electrons or particles labelled by the index p=$1, 2, 3...N_{sim}$ representing the sheet doping n_s of the graphene sheet is followed in time as they perform a random walk in the two dimensional $k_x - k_y$ space. Each electron undergoes a series of free flights and scatterings as usual and the energy and momentum of each electron is updated after each scattering event. The time domain is discretized into small time steps of length Δt and the real space of the device (labelled as z) is discretized into small space steps of length Δz. The direction of the applied electric field F is assumed to be y. The EMC simulator for graphene can be summarized as follows.

- Initialize all particles according to a Maxwellian distribution at t=0
- In a time step Δt, each particle in the ensemble p=$1, 2, 3...N_{sim}$ undergoes a series of free flights of duration $t_f(p)$ and scattering events. The k_y for each particle is updated according to $k_y(p) = k_y(p) - eFt_f(p)/\hbar$.
- Free flights are generated using a uniform random number $r_1 \sim U[0, 1]$ and $t_f(p) = -ln(r_1)/(\Gamma_t)$.
- The total scattering rate for each particle $\Gamma_p(k)$ can be found by summing the scattering rates due to all the mechanisms which have been detailed in section 5.3, $\Gamma_p(k) = \frac{1}{\tau}^{ac}(k) + \frac{1}{\tau}^{LA/TA}(k) + \frac{1}{\tau}^{LO/TO}(k)$.
- The total scattering rate is made independent of k by adding a large fictitious scattering rate called self-scattering Γ_{ss}, i.e., $\Gamma_t = \Gamma_{ss} + \Gamma_p(k)$.
- Γ_t is normalized to 1 and another uniform random number $r_2 \sim U[0, 1]$ is generated to randomly select the appropriate scattering mechanism according to their respective weights.
- The scattering energy exchange ΔE_{scatt} for acoustic phonon scattering is $\Delta E_{scatt,ac} = 0$ while for optical phonons it is $\Delta E_{scatt,op} = \pm\hbar\omega_0$. The energy of the p-th particle is updating according to $E_p = \hbar k_p v_F + \Delta E_{scatt}$.

- The momentum is updated according to, $k_p = \frac{E_p}{\hbar v_F}$.
- As all the scattering mechanisms in section 5.3 are deformation potential scatterings which randomize the momentum completely, another uniform random number is generated $r_3 \sim U[0,1]$. Then k_x and k_y are updated according $k_{x,p} = k_p \cos(2\pi r_3)$ and $k_{y,p} = k_p \sin(2\pi r_3)$.
- At the end of each time step, Poisson's equation is solved using the methods described in section 2.5 of chapter 2.
- The simulation ends when all the observable dynamical quantities such as the current and electron density have reached their steady state values and no longer have any significant changes over time.

5.5 Negative differential resistance in suspended graphene

Negative differential resistance (NDR) has been studied in suspended graphene [57, 58, 61]. The existence of NDR is an interesting phenomenon and could be useful for a wide range of applications.

A single layer of suspended graphene is simulated using graphene's scattering rates as the input to the EMC model described in section 5.4. The graphene layer is n-doped to 5x10^{11} cm^{-2}. The steady state drift velocity as a function of the applied D.C electric field for suspended graphene at room temperature is illustrated in Fig. 5.4.

As can be seen from Fig. 5.4, graphene exhibits ultra high low field mobility and NDR with a peak velocity of 6.5 x 10^5 m/s at an electric field of 1 kV/cm. The drift velocities in graphene are 4-5 times higher than the drift velocities of most III-V compounds which exhibit NDR.

5.6 Proposed Graphene Oscillator

A device structure with an n-doped layer of suspended graphene sandwiched between two n^+ regions of graphene as illustrated in Fig. 5.5 is proposed. Such device structures are commonly used in microwave oscillators employing

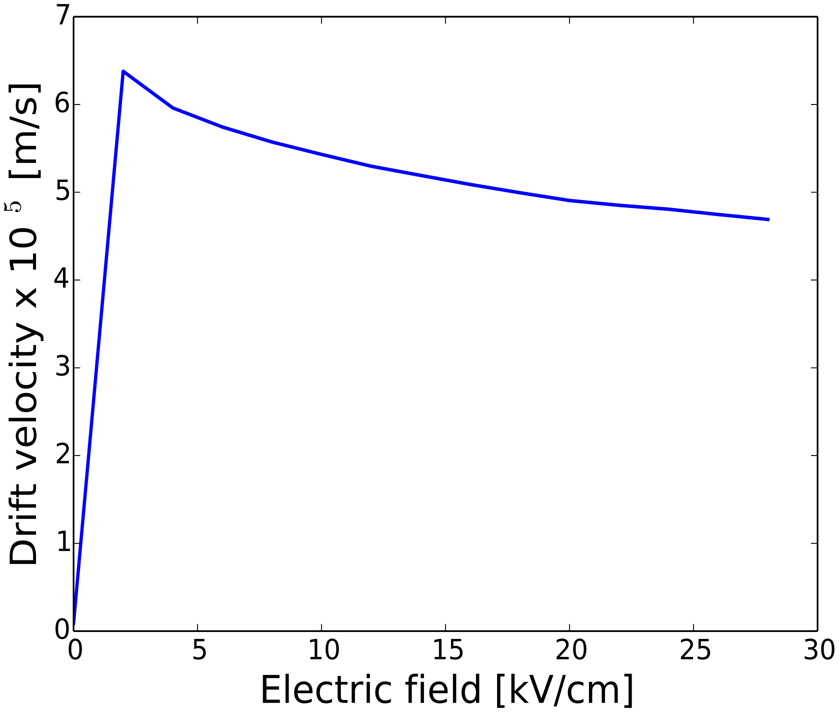

Figure 5.4: Monte Carlo simulation of drift velocity as a function of applied electric field for suspended graphene at 300 K.

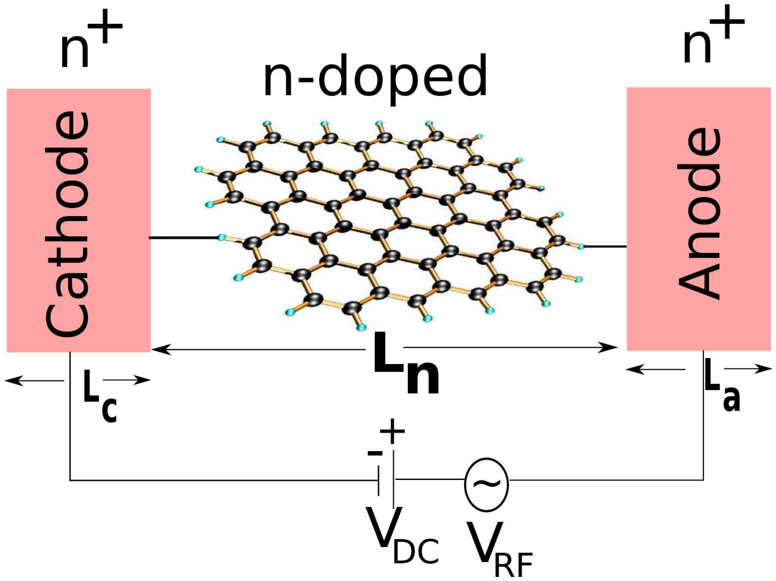

Figure 5.5: Proposed device structure using a layer of doped suspended graphene between two heavier doped regions with an applied voltage.

III-V compounds [63]. Typically, a D.C. voltage V_{DC} sufficient enough to bias the graphene sheet in its NDR region is applied. The design and simulation parameters for the device in Fig. 5.5 are listed in Table 5.1.

The effective thickness t_d is used to convert the sheet doping of 2D graphene into volume doping which is needed to use Poisson's equation. Space charge effects are essential in capturing the operation of oscillators which operate in regimes which are far from equilibrium. The self consistent Monte Carlo-Poisson solver has been a cornerstone of semiconductor device simulation in non-equilibrium and transient regimes for nearly three decades [64]. In order to mimic the wave guide cavity and circuit, a time varying sinusoidal RF voltage V_{RF} is applied in addition to the D.C electric field and takes the form $V_{RF} sin(2\pi f_{RF} t)$ [63, 65]. Realistic boundary conditions are used in the simulation of the graphene oscillator. In the simulation of QCLs, periodic boundary conditions were assumed because three stages of the device were being simulated and the first and third stage merely acted as boundaries and hence the central stage which is the simulated device was not affected by the boundary conditions. For the graphene oscillator, elec-

Table 5.1: Design and simulation parameters for proposed graphene oscillator design at 300 K.

Parameter	**Value**
Relative dielectric constant	10
Active/ region sheet doping n [cm^{-2}]	5x10^{11}
Cathode and anode sheet doping n^+ [cm^{-2}]	5x10^{12}
Effective thickness t_d [cm]	2x10^{-5}
Number of simulated electrons N_{sim}	4x10^{5}
D.C electric field [kV/cm]	30
Length of active region L_n [μm]	1.0
Length of cathode L_c [μm]	0.1
Length of anode L_a [μm]	0.2
R.F voltage V_{RF} [V]	1.0
R.F frequency f_{RF} [GHz]	640
Time step of Monte Carlo simulator Δt [fs]	0.1
Space step for Poisson equation solver Δz [μm]	0.005

trons are injected according to a thermalized, room temperature Maxwellian distribution when they exit the cathode or the anode corresponding to an energy of k_BT since graphene is a 2D material.

5.6.1 Simulation results

The final simulated device current (in absolute units) is plotted against the applied voltage in Fig. 5.6 for two RF periods. For the exact calculation of the current, one would simply need to multiply the current density with the width of the graphene sheet.

The generation of THz power is due the negative resistance of the oscillator. The negative resistance is a consequence of a phase shift between the current and voltage as can be seen in Fig. 5.6. The method for estimating whether the oscillator offers a negative resistance or not is briefly described now. The R.F. voltage is a sinusoidally varying signal with a time period T and angular frequency $\omega = 2\pi f_{RF}$. The sinusoidally averaged current over one period is given by,

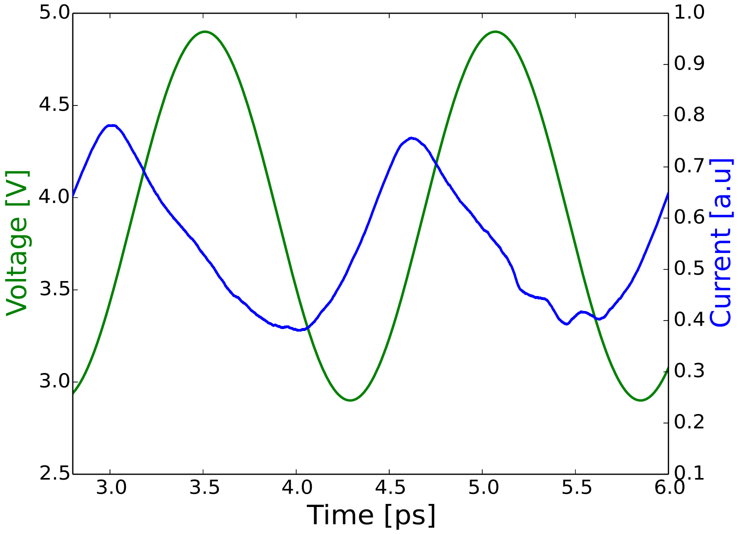

Figure 5.6: Simulated device current plotted against the applied voltage for the proposed device at 300 K.

$$\langle I \rangle = \frac{2}{T} \int_0^T I(t) sin(\omega t) dt. \tag{5.8}$$

The device resistance is given by $R_D = V_{RF}/\langle I \rangle$ and for the oscillator it is indeed negative $R_D < 0$. A capacitor, for example, would have a 90^o phase shift with respect to the voltage and this would have yielded a vanishing integral in Eq. (5.8), i.e., $\langle I_{capacitor} \rangle = 0$. A normal or positive resistor has no phase shift with respect to the voltage.

To extract the fundamental frequency (first harmonic) of the oscillating current, a fast Fourier transform (FFT) of the current is calculated and the relative magnitude of the power of the frequency spectrum is plotted as a function of the frequency in Fig. 5.7. As can be seen from Fig. 5.7, a clear peak at f_{osc}=0.641 THz or 641 GHz is observed corresponding to the oscillating frequency of the device. Another interesting feature is the presence of a second peak at approximately $2f_{osc}$ is also observed. This could potentially be leveraged for power generation at the second harmonic.

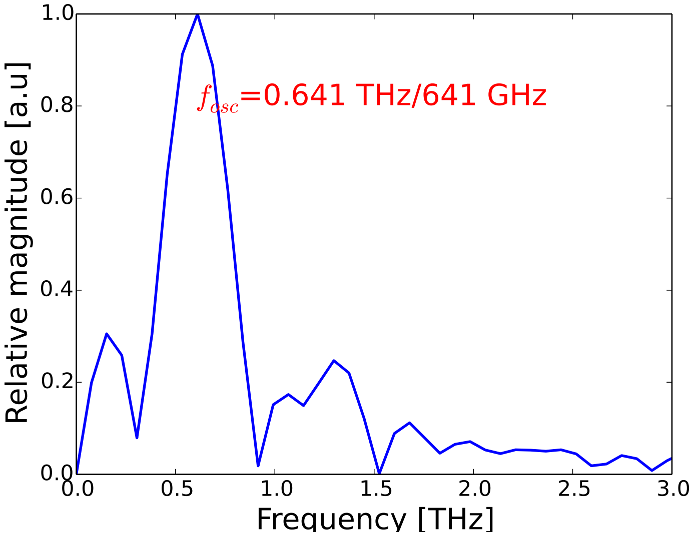

Figure 5.7: FFT of current showing a fundamental harmonic oscillating frequency of f_{osc}=0.641 THz.

In order to understand the physics behind the oscillations in the current, a few important microscopic variables of the device will now be illustrated and analyzed. The electron density along the device (with the doping density plotted in dashed lines) is plotted at various times during one RF period in Fig. 5.8. As can be seen from Fig. 5.8, the oscillation in the current (equivalently velocity) is due to the formation of space charge accumulation layers [65]. This is a consequence of the NDR that graphene exhibits and small space charge instabilities or excesses are amplified when the device is properly biased. During one RF period, accumulation layers or domains form close to the cathode and increase in magnitude as they transit the device and extinguish as they exit the anode. This cyclical or periodic nucleation and extinguishing of domains is the reason for the periodic oscillation in the current.

As a consequence of the space charge accumulation layers, the electric field inside the device also evolves in a periodic manner and are illustrated in Fig. 5.9. The electric field profiles are plotted at the same times at which the electron densities have been plotted in Fig. 5.9. As can be seen from

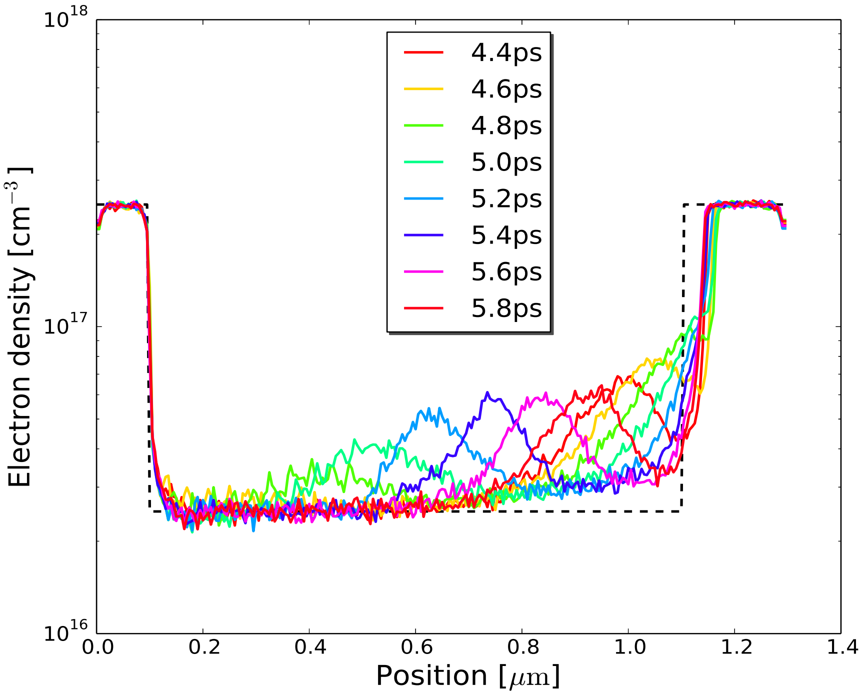

Figure 5.8: Simulated device electron density plotted at various times during one RF period.

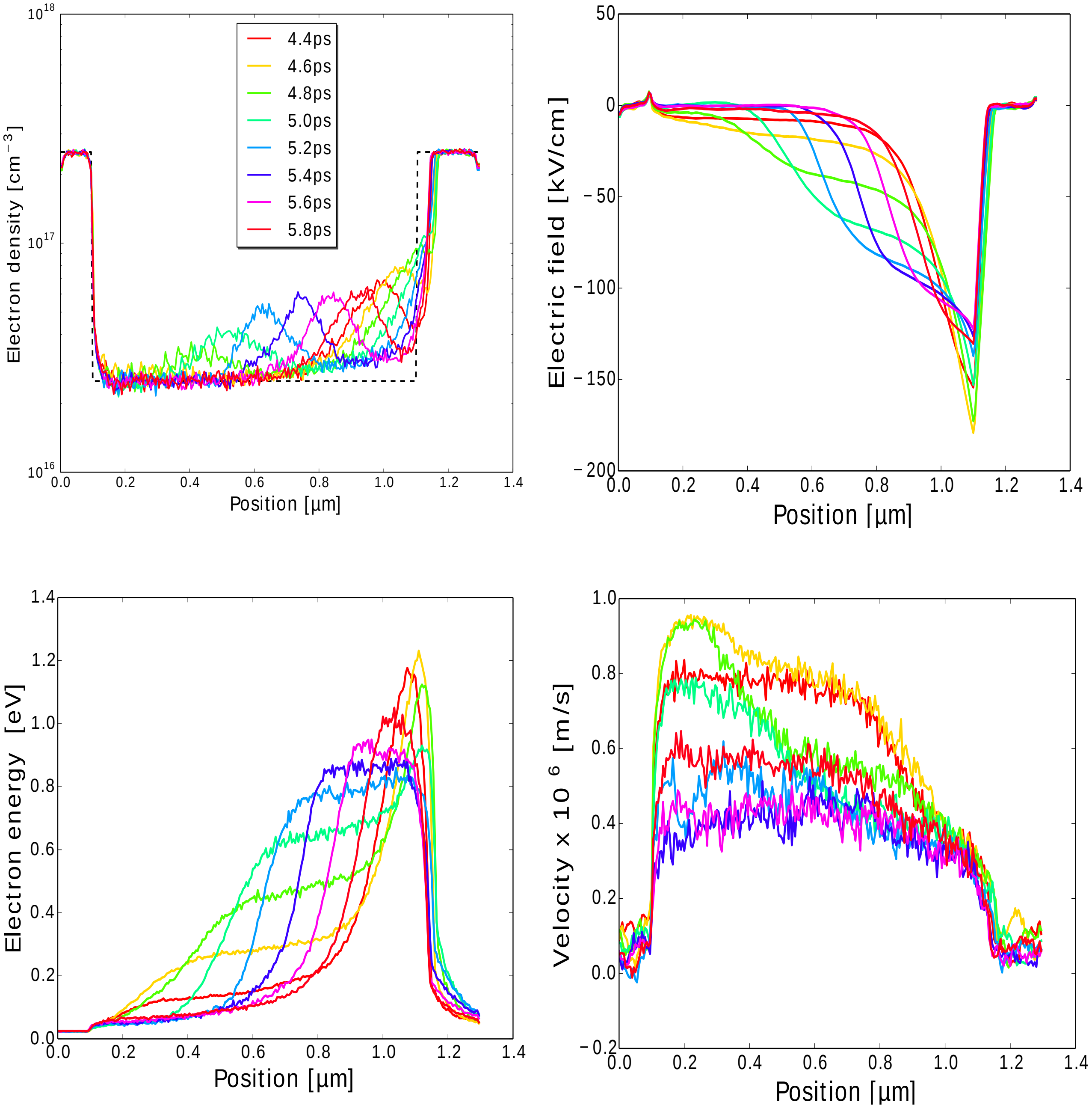

Figure 5.9: Electron densities, electric field profiles, average electron energies and velocities across the device plotted at various times during one RF period.

Fig. 5.9, the electric field is low in the contact regions and becomes positive and very small before the accumulation layer (in space) and increases to a large negative value in the space after the accumulation layer has peaked. This is a consequence of the "slowing down" of electrons due to their gain in mass. As the electric field becomes more negative, electrons which follow the dispersion relation $E = \hbar k v_F$ in graphene, gain energy and consequently their wavevector is increased. This increase in wavevector leads to an increase in effective mass according to the equation derived before, i.e., $m^*(k) = \frac{\hbar k}{v_F}$.

The spatial variations in the device of the average energy of the electrons and their velocities (at the same time instants at which the electron densities and electric fields have been illustrated) are also plotted in Fig. 5.9. The spatial trends in the energy and velocity profiles can be understood by observing the corresponding electric field profiles. As the electric field becomes larger and more negative, the electrons gain energy due to the increasing electric field and the acceleration of k_y and k. This gain in k leads to a increase in mass and decrease in velocity at larger electric fields.

5.6.2 0.8 μm active region device

In order to investigate if the proposed device concept could potentially oscillate at higher frequencies, the active region was shortened to $L_n = 0.8$ μm in order to reduce the transit time of the accumulation layers. This can be understood by approximating the oscillation frequency of the oscillator according to $f_{osc} = \frac{v_{tr}}{L_{tr}}$. v_{tr} can be rationalized as the average transit velocity of the accumulation layers and it depends on the applied bias and the corresponding electric fields. Also, in order to increase the velocity of the accumulation layers, the device bias is modified to 20 kV/cm corresponding to a higher velocity in the NDR region of graphene as can be seen in 5.5.

The simulated device current for this device is plotted in Fig. 5.10 and like the 1.0 μm device, the current and voltage are also out of phase as expected. The frequency spectrum computed using the FFT is plotted in Fig. 5.11. As can be seen from Fig. 5.11, a clear peak exists around f_{osc}=0.8 THz.

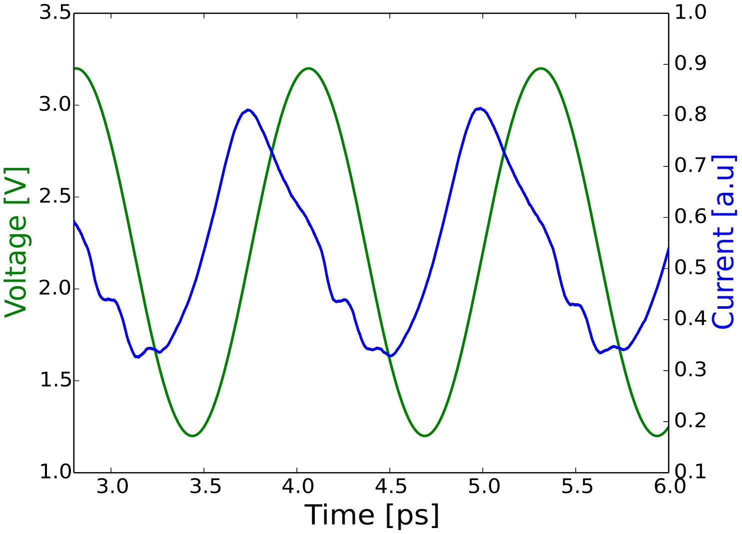

Figure 5.10: Simulated device current plotted against the applied voltage for the proposed device with 0.8 μm active region at 300 K.

5.7 Summary

In this chapter, the motivation for a fundamental THz source and the important applications it could facilitate were first outlined. Then the proposal of a novel electronic oscillator based on a single layer of suspended graphene were outlined. First, graphene's band structure was quantified along with the various scattering mechanisms involved in the electron transport of graphene. NDR in graphene was observed during the Monte Carlo simulation of its steady state v-F characteristics leading to the potential for high frequency oscillations due to graphene's higher velocities particularly when compared to III-V compounds. The Monte Carlo-Poission solver was used to simulate a 1.0 μm device and simulations showed oscillations in the current at 0.641 THz or 641 GHz. To probe whether the device concept could oscillate at higher frequencies, the active region was then shortened to 0.8 μm and simulation results showed an oscillation frequency of 0.8 THz.

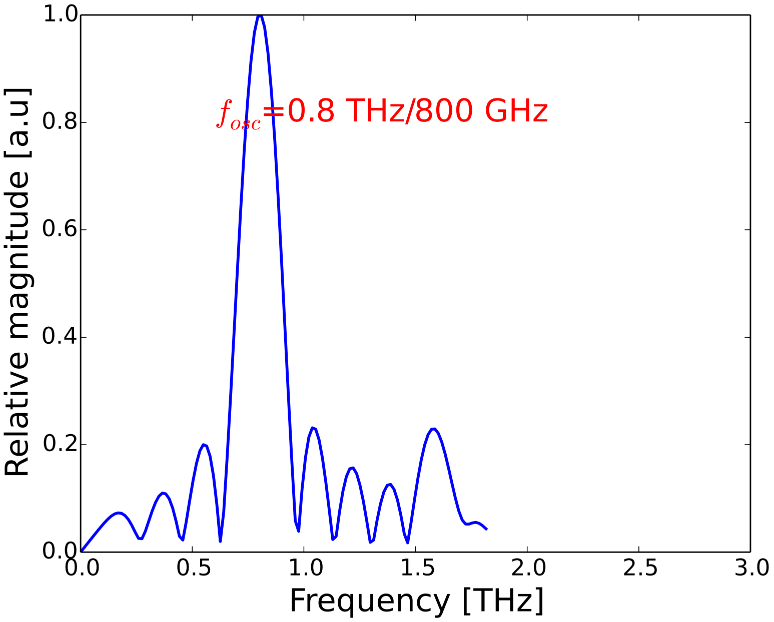

Figure 5.11: FFT of current showing a fundamental harmonic oscillating frequency of f_{osc}=0.8 THz for device with 0.8 μm active region .

Chapter 6

Conclusions and Future Work

In Part I of this dissertation, a quantitative and thorough framework for modeling mid-infrared QCLs and graphene based terahertz oscillators has been presented. As a result of precise wavefunction engineering, a novel long wavelength injectorless QCL emitting in the mid-infrared range was proposed. The performance of this compact design architecture yielded higher gain, characteristic temperature and wall plug efficiency when compared to previous designs which were based on the resonant tunneling paradigm for injector transport. In Part II of this dissertation, a novel room temperature fundamental THz source based on an electronic oscillator employing suspended single layer graphene was proposed. The EMC simulator outlined in Part I was adapted to model transport in graphene. The initial EMC simulations showed that graphene exhibits NDR and with velocities 4-5 times higher than III-V semiconductors which also display NDR. The high velocities and NDR were promising signs that this device concept could be used as high frequency electronic oscillator. And indeed, this device exhibited promising results oscillating in the range of 0.6-0.8 THz. The microscopic physics of this oscillator were then explained in detail. To the best of our knowledge, this is the first utilization of suspended graphene's NDR to produce such high frequency terahertz oscillations.

Future work in the area of long wavelength mid-infrared QCLs should involve a unified framework capturing the essential physics of the waveguide and thermal modeling of the complete laser. In particular, temperature dependent waveguide losses [36] are important to accurately compute the current densities and optical power of the QCL. Self-consistent electro-thermal modeling [50] is an active area of research for many electronic devices and a complete self-consistent electron-phonon transport model should be incorporated to study active region heating and different heat sink materials. Also, the optimization of the QCL structure can be performed and this can be carried by using evolutionary and genetic optimization algorithms such as the CMA-ES method which have been performed by the author of this dissertation for optical waveguides [66].

For the practical realization of the graphene oscillator, the dynamics of the device in a realistic resonant circuit need to be studied. In particular, the formulation of an equivalent circuit and modeling the various active and passive elements of the graphene oscillator in a resonant circuit need to be carried out [65]. The contacts in graphene devices could potentially be Schottky contacts and not Ohmic ones as in this thesis. The modeling of Schottky contacts is a challenging task and would represent an interesting challenge. The inclusion of a self-consistent electro-thermal model and the use of a full non-linear bandstructure model would make the modeling framework more thorough as well.

Bibliography

[1] D. Caffey *et al.*, “Recent Results from Broadly Tunable External Cavity Quantum Cascade Lasers”, *Presentation 7953-54. Photonics West* `http://www.daylightsolutions.com/assets/003/5309.pdf` (2011)

[2] J. Faist *et al.*, “Quantum cascade laser”, *Science*, **264**, 553 (1994)

[3] A.J. Huber *et al.*, “Terahertz Near-Field Nanoscopy of Mobile Carriers in Single Semiconductor Nanodevices”, *Nano Letters*, **8**, 3766 (2008)

[4] K. Ishigaki *et al.*, “Direct intensity modulation and wireless data transmission characteristics of terahertz-oscillating resonant tunnelling diodes”, *Electronics Letters*, **48** (2012)

[5] R. Kazarinov and R. Suris, “Amplification of electromagnetic waves in a semiconductor superlattice, ”, *Sov. Phys., Semicond.*, **5**, 707 (1971)

[6] G.N. Rao and A. Kapf , “External cavity tunable quantum cascade lasers and their applications to trace gas monitoring”, *Applied optics*, **50**, A100 (2011)

[7] A. Bismuto *et al.*, “Electrically tunable, high performace quantum cascade laser”, *Appl. Phys. Lett.*, **96**, 141105 (2010)

[8] Y. Yao *et al.*, “A widely voltage-tinable quantum cascade laser based on two-step coupling”, *Appl. Phys. Lett.*, **95**, 021105 (2009)

[9] S. Luryi and M. Gouzman, “Feasibility of an optical frequency modulation system for free-space optical communications”, *International journal of high speed electronics*, **16**, 559 (2006)

[10] A. Wittman *et al.*, " Distributed-feedback quantum-cascade lasers at 9 μm operating in continuous wave up to 423 K", *IEEE Photonics Tech. Lett.*, **21**, 814 (2009)

[11] S. Kumar *et al.*, "186 K operation of terahertz quantum-cascade lasers based on a diagonal design", *Appl. Phys. Lett.*, **94**, 131105 (2009)

[12] R. Terazzi and J. Faist, "A density matrix model of transport and radiation in quantum cascade lasers", *New Journal of Physics*, **12**, 033045 (2010)

[13] C. Weber *et al.*, "Density-matrix theory of the optical dynamics and transport in quantum cascade structures:The role of coherence", *Phys. Rev. B*, **79**, 165322 (2009)

[14] A. Matyas *et al.*, "Carrier transport in THz quantum cascade lasers: Are Green's functions necessary?", *IOP Journal of Physics:Conference Series*, **193**, 012026 (2009)

[15] G. Bastard, *Wave mechanics applied to semiconductor heterostructures*, Wiley series in monographs of physics, John Wiley and Sons, Chichester (1990)

[16] J.D. Cooper *et al.*, "Finite difference method for solving the Schrödinger equation with band nonparabolicity in mid-infrared quantum cascade lasers", *J. Appl. Phys.*, **108**, 113109 (2010)

[17] P.A. Dirac, "The Quantum Theory of Emission and Absorption of Radiation " *Proc. Roy. Soc. (London) A 114* , **767**, 243 (1927)

[18] A. Valavanis, PhD thesis, Institute of Microwaves and Photonics, School of Electronic and Electrical Engineering, University of Leeds (2009)

[19] S.M. Goodnick and P. Lugli, "Effect of electron-electron scattering on nonequilibrium transport in quantum-well systems", *Phys. Rev. B*, **37**, 2578 (1988)

[20] R.C. Iotti and F. Rossi, "Microscopic theory of semiconductor-based optoelectronic devices", *Rev. Prog. Phys*, **68**, 2533 (2005)

[21] R.C. Iotti and F. Rossi, "Nature of Charge Transport in Quantum-Cascade Lasers", *Phys. Rev. Lett*, **87**, 146603 (2001)

[22] C. Jacoboni and P. Lugli, *The Monte Carlo Method for Semiconductor Device Simulation*, Springer-Verlag, Vienna (1989)

[23] D. Vasileska, "Direct Solution of Boltzmann Transport Equation: Monte Carlo Method", `http://nanohub.org/resources/9111/download/monte_carlo.pdf`

[24] I. Vurgaftman *et al.*, "Band parameters for III-V compound semiconductors and their alloys", *J. Appl. Phys.*, **89**, 5815(2001)

[25] L. Shifren and D.K. Ferry, "A Wigner Function Based Ensemble Monte Carlo Approach for Accurate Incorporation of Quantum Effects in Device Simulation", *Journal of computational electronics*, **1**, 55 (2002)

[26] C. Jirauschek, "Monte Carlo study of carrier-light coupling in terahertz quantum cascade lasers", *Appl. Phys. Lett.*, **96**, 011103 (2010)

[27] J. Faist, F. Capasso, D. L. Sivco, C. Sirtori, A. L. Hutchinson, and A. Y. Cho, Science **264**, 553 (1994).

[28] M. Razeghi, New J. Phys. **11**, 125017 (2009).

[29] S. Katz, A. Vizbaras, R. Meyer, and M. C. Amann, J. Appl. Phys. **109**, 081101 (2011).

[30] P. Q. Liu, A. J. Hoffman, M. D. Escarra, K. J. Franz, J. B. Khurgin, Y. Dikmelik, X. Wang, J.-Y. Fan, and C. F. Gmachl, Nat. Photonics **4**, 95 (2010).

[31] Y. Bai, S. Slivken, S. Kuboya, S. R. Darvish, and M. Razeghi, Nat. Photonics **4**, 99 (2010).

[32] S. Katz, A. Vizbaras, G. Boehm, and M-C. Amann, Semicond. Sci. Technol. **26**, 014018 (2011).

[33] Kale J. Franz, *New quantum cascade laser architectures: II-VI quantum cascade emitters, high k-space lasing, and short injectors*, Princeton University (2009).

[34] G. L. Bir and G. Pikus, *Symmetry and Strain-Induced Effects in Semiconductors*, Wiley, New York (1974)

[35] C. G. Van de Walle, “Band lineups and deformation potentials in the model-solid theory, *Phys. Rev. B*, **39**, 1871 (1989).

[36] C. A. Evans, D. Indjin, and Z. Ikonic, J. Comput. Electron. **11**, 137 (2012).

[37] M. Yamanishi, K. Fujita, T. Edamura, and H. Kan, Opt. Express **16**, 20748 (2008).

[38] E. Dupont, S. Fathololoumi, Z. R. Wasilewski, G. Aers, S. R. Laframboise, M. Lindskog, S. G. Razavipour, A. Wacker, D. Ban, and H. C. Liu, J. Appl. Phys. **111**, 073111 (2012).

[39] S. Katz, A. Friedrich, G. Boehm, and M. C. Amann, Appl. Phys. Lett. **92**, 181103 (2008).

[40] A. Friedrich, G. Scarpa, G. Boehm, and M. C. Amann, Electronics Letters **41**, 529 (2005).

[41] M.V. Kisin *et al.*, “Proposal for Electrically Tunable Quantum-Cascade Laser”, *IEEE Photonics Technology Letters*, **19**, 426 (2007)

[42] J. D. Cooper, A. Valavanis, Z. Ikonic, P. Harrison, and J. E. Cunningham, J. Appl. Phys. **108**, 113109 (2010).

[43] C. Jirauschek, Appl. Phys. Lett. **96**, 011103 (2010).

[44] C. Jirauschek and P. Lugli, J. Appl. Phys. **105**, 123102 (2009).

[45] A. Matyas, P. Lugli, and C. Jirauschek, J. Appl. Phys. **110**, 013108 (2011).

[46] P. Borowik, J. L. Thobel, and L. Adamowicz, J. Appl. Phys. **108**, 073106 (2010).

[47] A. Matyas, S. Sontges, P. Lugli, C. Jirauschek, S. Katz, A. Vizbaras, and M. C. Amann, Computational Electronics (IWCE), 2010 14th International Workshop on, **12**, 1-4, (2010).

[48] R. C. Iotti and F. Rossi, Appl. Phys. Lett **78**, 2902 (2001).

[49] Z. Liu, C. F. Gmachl, L. Cheng, F. S. Choa, F. J. Towner, X. Wang, and J. Fan, IEEE J. Quantum Elect. **44**, 485 (2008).

[50] Y. B. Shi, Z. Aksamija, and I. Knezevic, J. Comput. Electron. **11**, 144 (2012).

[51] A. Matyas, M. A. Belkin, P. Lugli, and C. Jirauschek, Appl. Phys. Lett. **96**, 201110 (2010).

[52] J. Maloney *et al.*, "Compact, high-power, room-temperature, narrow-line terahertz source", DOI:10.1117/2.1201102.003523 (2011)

[53] J. Du *et al.*, "Terahertz imaging at 77 K", *Supercond. Sci. Technol.*, **22**, 114001 (2009)

[54] T. Kashiwagi *et al.*, "Efficient Fabrication of Intrinsic-Josephson-Junction Terahertz Oscillators with Greatly Reduced Self-Heating Effects", *Physical review applied*, **4**, 054018 (2015)

[55] R. Van Zyl *et al.*, "The Gunn-diode: fundamentals and fabrication", *Communications and Signal Processing, Proceedings of the 1998 South African Symposium on, Rondebosch*, **407-412** (1998)

[56] V. Dorgan *et al.*, "High-Field Electrical and Thermal Transport in Suspended Graphene", *Nano Letters*, **13(10)**, 4581 (2013)

[57] X. Li *et al.*, "Surface polar phonon dominated electron transport in graphene", *Appl. Phys. Lett.*, **97**, 232105 (2010)

[58] X. Li *et al.*, "First-principles analysis of electron-phonon interactions in graphene", *Phys. Rev. B*, **81**, 121412(R) (2010)

[59] D. Dissanayake *et al.*, "Spontaneous and strong multi-layer graphene n-doping on soda-lime glass and its application in graphene-semiconductor junctions", *Scientific reports*, **6**, 21070 (2016)

[60] B.K. Ridley and T.B. Watkins, "The Possibility of Negative Resistance Effects in Semiconductors", *Proceedings of the Physical Society*, **78**, 293 (1961)

[61] R.S. Shishir and D.K. Ferry, "Velocity saturation in intrinsic graphene", *J. Phys. Condens. Matter*, **21**, 344201 (1961)

[62] R. Rengel *et al.*, "A Monte Carlo Study of Electron Transport in Suspended Monolayer Graphene", *Spanish Conference on Electron Devices*, 175 (2013)

[63] R. Kamoua *et al.*, "D-BAND (ll0-170GHz) InP GUNN DEVICES", *Solid-state electronics*, **36**, 1547 (1993)

[64] M.V. Fischetti and S.E. Laux, "Monte carlo analysis of electron transport in small semiconductor devices including band-structure and space-charge effects", *Phys. Rev. B*, **38**, 9721 (1988)

[65] R. Kamoua, "Monte Carlo-Based Harmonic-Balance Technique for the Simulation of High-Frequency TED Oscillators", *IEEE Transactions on microwave theory and techniques*, **46**, 1376 (1998)

[66] S. Singh *et al.*, "An MMI-based wavelength combiner employing non-uniform refractive index distribution", *Optics Express*, **22**, 8533, (2014)

[67] A.H. Castro Neto *et al.*, "The electronic properties of graphene", *Reviews of Modern Physics*, **81**, 109 (2009)

[68] W. H. Press, S. A. Teukolsky, W. T. Vetterling, and B. P. Flannery, "Numerical Recipes in C", Cambridge, 2nd edition, 1997, ISBN 0-521-43108-5.

[69] `http://www.diva-portal.org/smash/get/diva2:721093/FULLTEXT01.pdf`

[70] `http://www.ece.utah.edu/~ece6340/LECTURES/Jan30/`

Appendices

Appendix A

Time Independent Schrödinger's Equation Solver

The stationary electronic wavefunctions for a quantum well heterostructre with a potential $V(z)$ (with z as the growth direction) are described by the time independent Schrödinger's equation (TISE),

$$-\frac{\hbar^2}{2}\frac{\partial}{\partial z}\left(\frac{1}{m^*(z)(1+\alpha(z)[E-V(z)])}\frac{\partial\psi}{\partial z}\right)+V(z)\psi(z)=E\psi(z). \tag{A.1}$$

The non-parabolicity factor $\alpha(z)$ and the energy dependent effective mass $m^*(E,z)$ is,

$$\alpha(z)=\frac{\beta(z)}{E_g(z)}\left(1-\frac{m^*(z)}{m_0}\right) \tag{A.2}$$

$$\beta(z)=\frac{1+4x(z)+2x^2(z)}{1+5x(z)+2x^2(z)} \tag{A.3}$$

$$x(z)=\frac{\Delta_{so}(z)}{E_g(z)}. \tag{A.4}$$

$$\frac{1}{m^*(E,z)}=\frac{1}{m^*(z)(1+\alpha(z)[E-V_c(z)])}. \tag{A.5}$$

The solution of Eq. (A.1) gives the energy eigenstates E and the corresponding eigevectors are the electron wavefunctions $\psi(z)$.

In order to solve Eq. (A.1), a finite difference solver was implemented using the method presented in [16]. This TISE is a non-linear and cubic eigen value problem (EVP) and this method linearizes the EVP into a sparse, banded an linear EVP albeit tripled in size [16]. This method was deemed computationally exhaustive for calculating the electronic states of quantum dots due to the three dimensional nature of a quantum dot's geometry [1] . However, for quantum well heterostructures such as QCLs, this method is computationally feasible.

Finite difference solver

The procedure outlined in [16] is adopted. Consider a discretization of the z-domain into a finite difference grid with a step size of δz. Let i be the index running over all the grid points. Intermediate points $(i \pm 1/2)$ are treated equal to the average of the two neighboring points i and $i \pm 1$. Infinite potential boundaries are considered at the simulation boundaries and the effective mass is defined by m for convenience and the superscript * has been removed . The finite difference (FD) discretization of the TISE with N grid points leads to (see Appendix D),

$$-\frac{\hbar^2}{2\delta z^2}\left\{\frac{\psi_{i+1}-\psi_i}{m_{i+1/2}[1+\alpha_{i+1/2}(E-V_{i+1/2})]}-\frac{\psi_i-\psi_{i-1}}{m_{i+1/2}[1+\alpha_{i-1/2}(E-V_{i-1/2})]}\right\}+V_i\psi_i = E\psi_i \tag{A.6}$$

Rearranging the terms to be in ascending order spatially ($i-1$ comes first followed by i and $i+1$), one can recast the above equation into a matrix equation in ascending orders of E and this takes the form,

$$(E^3\mathbf{A}_3 + E^2\mathbf{A}_2 + E\mathbf{A}_1 + \mathbf{A}_0)\psi = 0, \tag{A.7}$$

where $\psi = (\psi_1\psi_2...\psi_N)$ is a single dimensional array containing values of the wavefunction at every grid point in the discretization space. The matrices $\mathbf{A}_0$, $\mathbf{A}_1$, $\mathbf{A}_2$ and $\mathbf{A}_3$ are NxN matrices and are either tri-diagonal or diagonal. The exact form of the matrices and the elements of these matrices

---

[1] Hwang et al., Math. Comp. Modell., **40**, 519 (2004)

are now detailed. $\mathbf{A}_0$ and $\mathbf{A}_1$ are tri-diagonal matrices while $\mathbf{A}_2$, $\mathbf{A}_3$ are purely diagonal matrices.

$$\mathbf{A}_0 = \begin{bmatrix} b_1 & a_1 & 0 & \dots & 0 \\ a_1 & b_2 & a_2 & \dots & \vdots \\ 0 & \ddots & \ddots & \ddots & 0 \\ \vdots & \dots & a_{N-2} & b_{N-1} & a_{N-1} \\ 0 & \dots & 0 & a_{N-1} & b_N \end{bmatrix}$$

$$\mathbf{A}_1 = \begin{bmatrix} d_1 & c_1 & 0 & \dots & 0 \\ c_1 & d_2 & c_2 & \dots & \vdots \\ 0 & \ddots & \ddots & \ddots & 0 \\ \vdots & \dots & c_{N-2} & d_{N-1} & c_{N-1} \\ 0 & \dots & 0 & c_{N-1} & d_N \end{bmatrix}$$

$$\mathbf{A}_2 = \begin{bmatrix} e_1 & 0 & 0 & \dots & 0 \\ 0 & e_2 & 0 & \dots & \vdots \\ 0 & \ddots & \ddots & \ddots & 0 \\ \vdots & \dots & 0 & e_{N-1} & 0 \\ 0 & \dots & 0 & 0 & e_N \end{bmatrix}$$

$$\mathbf{A}_3 = \begin{bmatrix} f_1 & 0 & 0 & \dots & 0 \\ 0 & f_2 & 0 & \dots & \vdots \\ 0 & \ddots & \ddots & \ddots & 0 \\ \vdots & \dots & 0 & f_{N-1} & 0 \\ 0 & \dots & 0 & 0 & f_N \end{bmatrix}$$

The matrix elements are given by,

$$a_i = \frac{\hbar^2}{2\delta z^2} m_{i-1/2}(1 - \alpha_{i-1/2}V_{i-1/2}), \tag{A.8}$$

$$b_i = \frac{\hbar^2}{2\delta z^2}[-m_{i-1/2}(1 - \alpha_{i-1/2}V_{i-1/2}) - m_{i+1/2}(1 - \alpha_{i+1/2}V_{i+1/2})] \\ -(1-\alpha_{i-1/2}V_{i-1/2}-\alpha_{i+1/2}V_{i+1/2}-\alpha_{i-1/2}\alpha_{i+1/2}V_{i-1/2}V_{i+1/2})m_{i+1/2}m_{i-1/2}V_i, \tag{A.9}$$

$$c_i = \frac{\hbar^2}{2\delta z^2} m_{i-1/2}\alpha_{i-1/2} \tag{A.10}$$

$$d_i = \frac{\hbar^2}{2\delta z^2}(-m_{i-1/2}\alpha_{i-1/2} - m_{i+1/2}\alpha_{i+1/2}) + [1 - \alpha_{i-1/2}(V_{i-1/2} + V_i) \\ - \alpha_{i+1/2}(V_{i+1/2} + V_i) + \alpha_{i-1/2}\alpha_{i+1/2} \\ (V_{i-1/2}V_i + V_{i+1/2}V_i + V_{i+1/2}V_{i-1/2})]m_{i+1/2}m_{i-1/2}, \tag{A.11}$$

and

$$e_i = m_{i+1/2}m_{i-1/2}\alpha_{i+1/2}\alpha_{i-1/2}. \tag{A.12}$$

The matrix equation in Eq. (A.7) can now be converted into a normal EVP using the techniques described in [16].

Solver validation

In order to validate the solver, one can compare $\Delta E = E_{UL} - E_{LL}$ to the experimental peak luminiscence wavelength of an experimentally fabricated and tested QCL [7] and as can be seen from the following table, there is a good agreement between the experimental wavelengths and the wavelengths calculated using the finite difference solver.

$$\lambda = \frac{hc}{\Delta E}$$

Voltage bias (V)	$\lambda_{experimental}$ (μm)	$\lambda_{theoretical}$ (μm)
11.9	8.8256	8.7949
12.9	8.7819	8.6519
13.7	8.6411	8.3221

Appendix B

Fermi's Golden Rule

The time varying potentials $\hat{V}(t)$ are treated as small pertrurbations to $\hat{H}_0$. These perturbations perturb the state over time and the time varying state can be represented by a weighted sum of the unperturbed states given by,

$$|\psi(t)\rangle = \sum_{\phi} a_{\phi}(t)|\phi\rangle e^{\frac{-iE_{\phi}t}{\hbar}}. \tag{B.1}$$

Inserting this equation in the time-dependent Schrödinger equation,

$$\sum_{\phi} \Big(a_{\phi}(t)\hat{H}_0|\phi(t)\rangle + a_{\phi}(t)\hat{V}(t)|\phi(t)\rangle \Big) = i\hbar \sum_{\phi} \left[a_{\phi}(t)\frac{\partial}{\partial t}|\phi(t)\rangle + \frac{da_{\phi}(t)}{dt}|\phi(t)\rangle \right]. \tag{B.2}$$

The first parts on either side of the above equation represent the unperturbed system and therefore can be excluded. If one considers an electron in state $|\phi\rangle$ making a transition to a final state $|f\rangle$ one can write,

$$\sum_{\phi} a_{\phi}(t)\langle f|\hat{V}(t)|\phi\rangle e^{\frac{-iE_{f\phi}t}{\hbar}} = i\hbar \sum_{\phi} \frac{da_{\phi}(t)}{dt}\langle f|\phi\rangle, \tag{B.3}$$

where $E_{f\phi} = E_f - E_{\phi}$ is the total transition energy.

Employing the orthonormality of of states and defining $V_{\phi f(t)=\langle f|\hat{V}(t)}|\phi\rangle$,

$$\frac{da_f(t)}{dt} = \frac{1}{i\hbar}\sum_{\phi} a_{\phi}(t)V_{\phi f}(t)e^{\frac{-iE_{f\phi}t}{\hbar}} \tag{B.4}$$

Assuming that the scattering rates are small enough so that the electrons are likely to remain in their initial state $|i\rangle$ between two measurements, one can state that $a_\phi(t) = \delta_{i\phi}$ and that the probability of finding an electron in state $|f\rangle >$ is given by,

$$|a_f(t)|^2 = \frac{1}{\hbar^2}\left| \int_0^t V_{if}(t') e^{\frac{-iE_{f\phi}t}{\hbar}} dt' \right|^2 . \tag{B.5}$$

In QCLs, $E_{i/f}$ is the total energy of the electron and is explicitly given by a sum of the z component $E_{i/f}$ which is the minimum of the subband and the energy in the plane $E_{xy} = \frac{\hbar^2 {k_{i/f}}^2}{2m^*}$.

$$E_{i/f}(k_{i/f}) = E_{i/f} + \frac{\hbar^2 {k_{i/f}}^2}{2m^*} \tag{B.6}$$

where $k_{i/f}$ is the in-plane momentum of the electron in the initial(before scattering) and final subband(after scattering).

We can now study the various scattering mechanisms governing the electron dynamics in QCLs. Static scattering potentials $V_{if}(t) = V_{if}$ can in principle be included in the time independent Schrödinger equation for calculating the stationary electronic states but it is physically more intuitive to study them in conjecture with the time varying mechanisms. Hence we can broadly classify the scattering mechanisms into static and time varying potentials.

Static scattering potentials

For static scattering potentials,

$$|a_f(t)|^2 = \frac{{|V_{if}|}^2 t^2}{\hbar^2} sinc^2\left(\frac{E_{fi}t}{2\hbar}\right) \tag{B.7}$$

In the limit $t \to \infty$, i.e., the transients have died away and steady state has been reached, the above equation reduces to

$$\lim_{t\to\infty} |a_f(t)|^2 = \frac{2\pi}{\hbar} |V_{if}|^2 \delta(E_{fi}). \tag{B.8}$$

Thus the final state is only occupied for static potentials if the scattering is elastic or $E_f = E_i$. Differentiating the probability yields the scattering rate $\frac{1}{\tau_{if}}(k_i)$ transporting the electron from it's initial state $|i\rangle$ to a final state $|f\rangle$ [18]

$$\frac{1}{\tau_{if}}(k_i) = \frac{2\pi}{\hbar}|V_{if}|^2\delta(E_{fi}) \tag{B.9}$$

This is the famous ***Fermi's golden rule*** (FGR) [17]. [1]

Time varying potentials

The time varying potentials in semiconductors generally arise due to vibrating phonons. Electron-phonon scattering potentials can be represented by a sinusoidal perturbation and take the form,

$$V_{if}(t) = V_{if}\left(e^{j\omega_0 t} + e^{-j\omega_0 t}\right) \tag{B.10}$$

where ω_0 is the angular frequency of the oscillating potential due to the vibrating phonons.

In the steady state limit $t \to \infty$ we obtain the scattering rate as [18],

$$\frac{1}{\tau_{if}}(k_i) = \frac{2\pi}{\hbar}|V_{if}|^2\left[\delta(E_{fi} - \hbar\omega_0) + \delta(E_{fi} + \hbar\omega_0), \right] \tag{B.11}$$

where the + sign corresponds to absorption and the - sign to emission of a phonon.

---

[1] Although named after Enrico Fermi, it was Paul Dirac who had formulated this equation in his 1927 paper "The Quantum Theory of Emission and Absorption of Radiation" *Proc. Roy. Soc. (London) A* 114 (767): 243265

Appendix C

Graphene Bandstructure

Graphene is comprised of carbon atoms arranged in a hexagonal or honeycomb lattice as shown in Fig. C.1.

The bandstructure of graphene is derived using the approach from [67]. The notations of [67] will be followed and a tight-binding Hamiltonian with hopping energies used as fitting parameters will be used to drive the E-k dispersion of graphene.

The structure of graphene is a triangular lattice with a basis of two atoms per unit cell. The carbon-carbon distance is a=1.42 A^o. The lattice vectors in real space can be written as (Fig. C.2),

$$\mathbf{a_1} = \frac{a}{2}(3, \sqrt{3}) \quad \text{and} \quad \mathbf{a_2} = \frac{a}{2}(3, -\sqrt{3}). \tag{C.1}$$

The reciprocal lattice vectors (Fig. C.3) are there given by,

$$\mathbf{a_1} = \frac{a}{2}(3, \sqrt{3}) \quad \text{and} \quad \mathbf{a_2} = \frac{a}{2}(3, -\sqrt{3}). \tag{C.2}$$

The points at the corner of the Brillouin zone of graphene are labeled as the K and K' points and are of particular importance. These are called the Dirac points. Their positions in the reciprocal momentum space are given by,

$$\mathbf{K} = \left(\frac{2\pi}{3a}, \frac{2\pi}{3\sqrt{3}a}\right) \quad \text{and} \quad \mathbf{K'} = \left(\frac{2\pi}{3a}, -\frac{2\pi}{3\sqrt{3}a}\right). \tag{C.3}$$

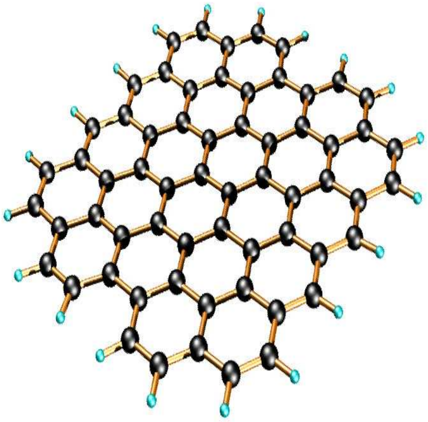

Figure C.1: Hexagonal honeycomb lattice of graphene. Figure from [69].

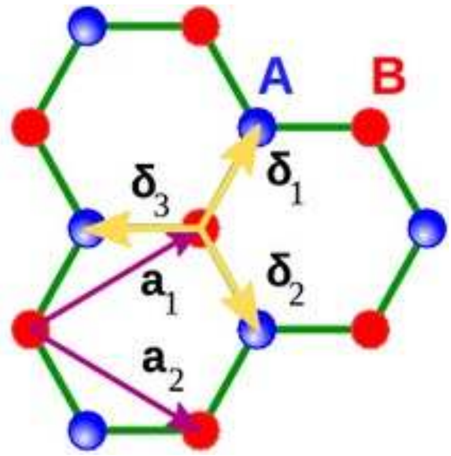

Figure C.2: Honeycomb lattice of graphene and its Brillouin zone. The lattice structure of graphene, made out of two inter-penetrating triangular lattices. a_1 and a_2 are the real-space lattice unit vectors. δ_i, i= 1, 2, 3 are the nearest-neighbor vectors. Figure from [67, 69].

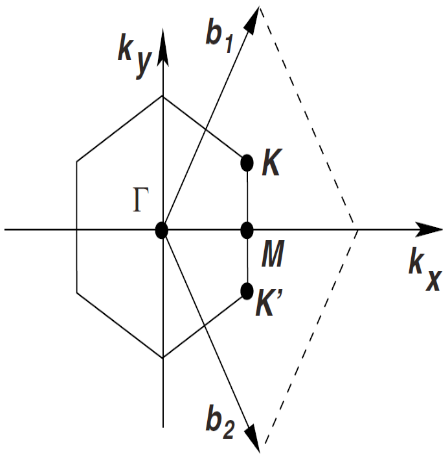

Figure C.3: Reciprocal lattice structure of graphene with basis vectors b_1 and b_2 along with various points in the Brillouin zone. Figure from [67, 69].

The three nearest-neighbor vectors in real space are,

$$\delta_{\mathbf{1}} = \frac{a}{2}(1, \sqrt{3}), \quad \delta_{\mathbf{2}} = \frac{a}{2}(1, -\sqrt{3}) \quad \text{and} \quad \delta_{\mathbf{3}} = -a(1, 0). \tag{C.4}$$

while the six second-nearest neighbors are located at $\delta'_1 = \pm\mathbf{a_1}$, $\delta'_2 = \pm\mathbf{a_2}$ and $\delta'_3 = \pm(\mathbf{a_2} - \mathbf{a_1})$.

The tight-binding Hamiltonian used in [67] with a nearest neighbor hopping energy of $t \approx 2.8$ eV and next nearest-neighbor hopping energy of $t' \approx 0.1$ eV leads to following energy bands (in units of $\hbar$=1),

$$E_{\pm}(\mathbf{k}) = \pm t\sqrt{3 + f(\mathbf{k})} - t' f(\mathbf{k}), \tag{C.5}$$

$$f(\mathbf{k}) = 2cos(\sqrt{3}k_y a) + 4cos(\frac{\sqrt{3}}{2}k_y a)cos(\frac{3}{2}k_x a). \tag{C.6}$$

The energy dispersion for graphene can now be plotted. The full bandstructure of graphene using Eq. (C.5) can now be plotted and is shown in Fig. C.4.

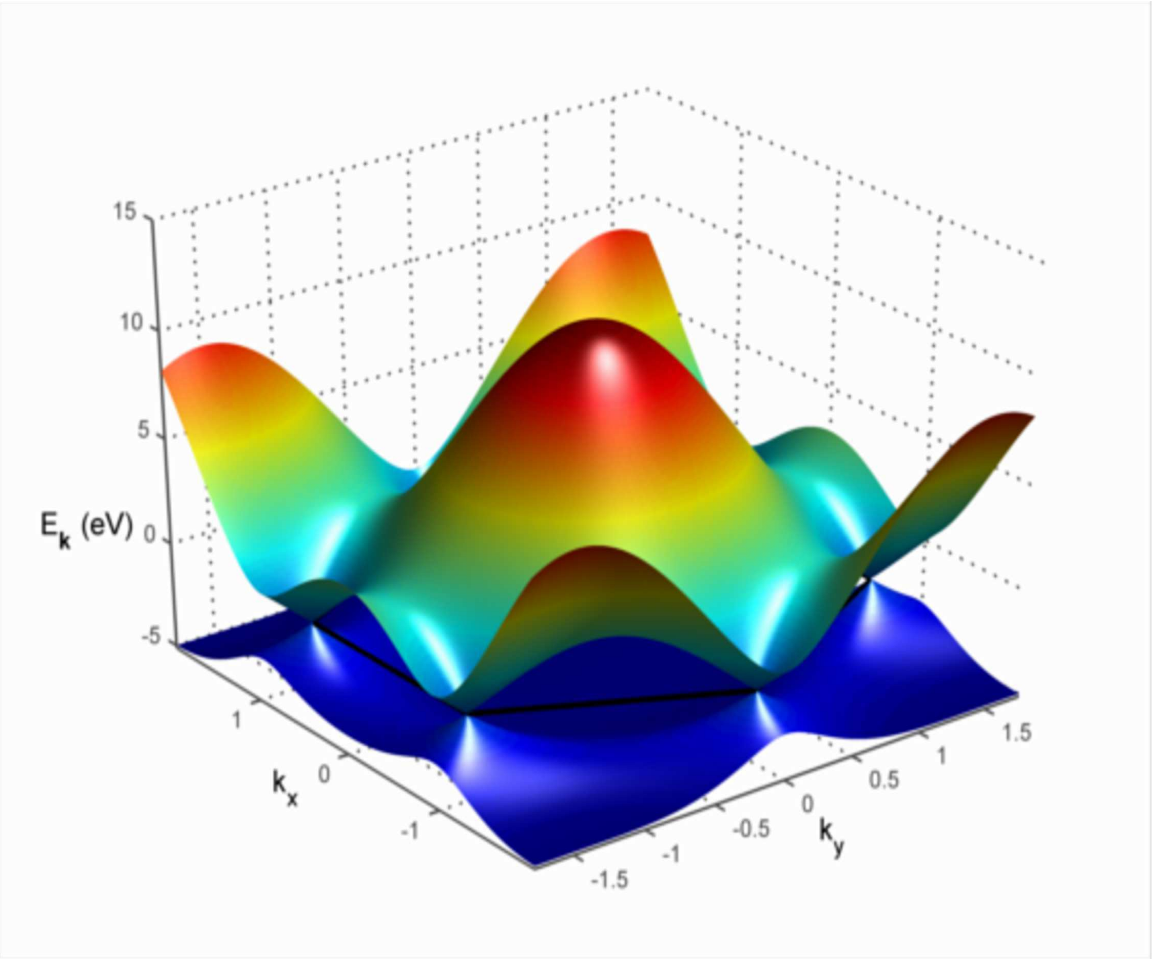

Figure C.4: E-k dispersion of graphene. Figure from [69].

Eq. (C.5) is the full band structure E-k dispersion for graphene. Close to the K or K' vector, as **k**=**K**+**q** with $|\mathbf{q}| << |\mathbf{K}|$,

$$E_{\pm}(\mathbf{q}) = \pm v_F |\mathbf{q}|. \tag{C.7}$$

Here the Fermi velocity is $v_F = 3ta/2$ and this value is clearly $v_F \approx 10^6$ m/s (rescaling v_F to be dimensionally correct by dividing it with $\hbar$) . **q** is the momentum measured relative to the Dirac points and hence can be though of as $|\mathbf{q}| = \hbar k$. An interesting feature to compare with materials with a parabolic E-k dispersion is that in their case, the Fermi velocity depends on the energy and is given by $v = \sqrt{\frac{2E}{m^*}}$.

The energy dispersion showing the linear E-k dispersion in the vicinity of the Dirac points can also be visualized in Fig. C.5. The cones that are formed by this dispersion are often referred to as Dirac cones.

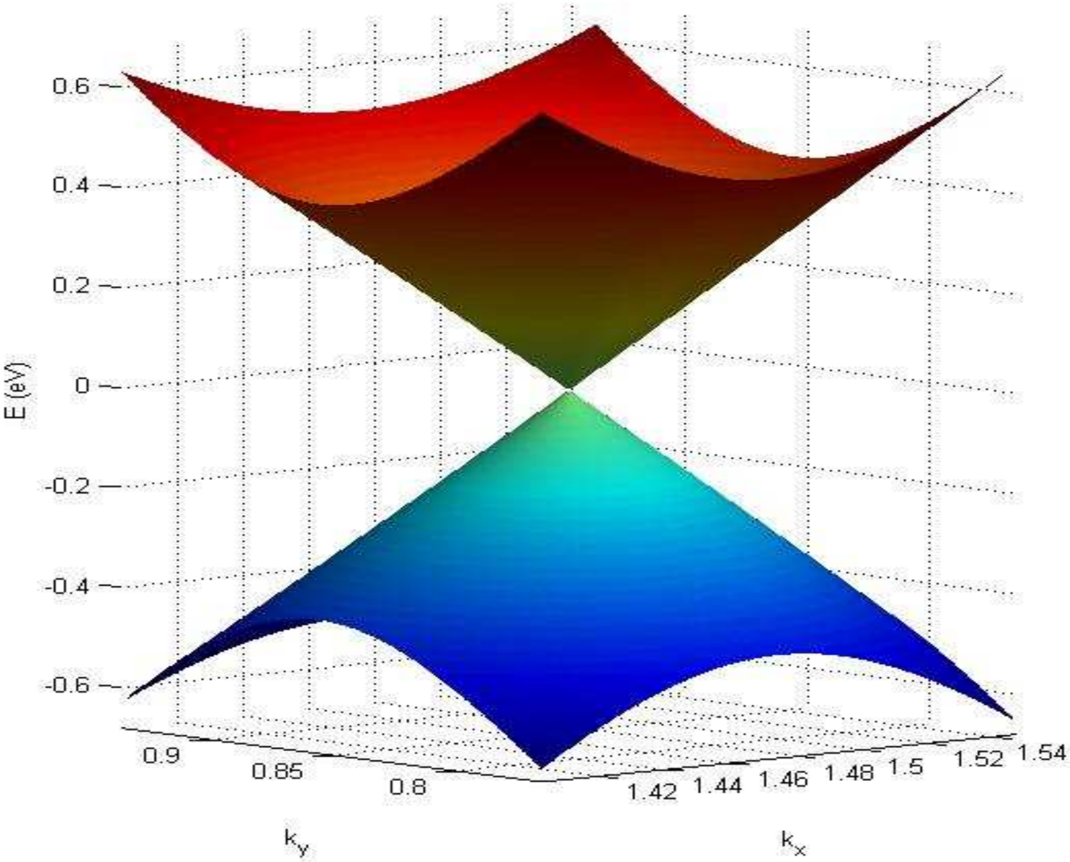

Figure C.5: E-k dispersion of graphene in the vicinity of the Dirac points. Figure from [69].

Appendix D

Numerical Differentiation and Integration

Finite difference approximations of derivative

Consider two smoothly varying functions $f(x)$ and $g(x)$. The domain of these functions can be discretized into a grid such as the one in Fig. D.1. The finite difference approximation of the generalized order derivative $\frac{d}{dx}(f(x)dg(x)/dx)$ evaluated at the point i is given by,

$$\frac{d}{dx}(f(x)g(x))|_i \approx \frac{1}{\Delta x}[f(i+1/2)(g(i+1)-g(i))-f(i-1/2)(g(i)-g(i-1))] \tag{D.1}$$

where $i = 1, 2, 3...n$ runs over all the grid points in the domain and $f(i)$ and $g(i)$ are the values of the respective functions at those grid points. The values at the intermediate points can be taken to be the averages of their nearest neighbors, i.e., $f(i \pm 1/2) = [f(i) + f(i \pm 1)]/2$.

1D Trapezoidal rule

The integral of a function $f(x)$ between two end points a and b can be approximated as the area under the curve $f(x)$ between a and b. This is called the 1D trapezoidal rule and is an numerical approximation of the integral $\int_a^b f(x)dx$ and is given by,

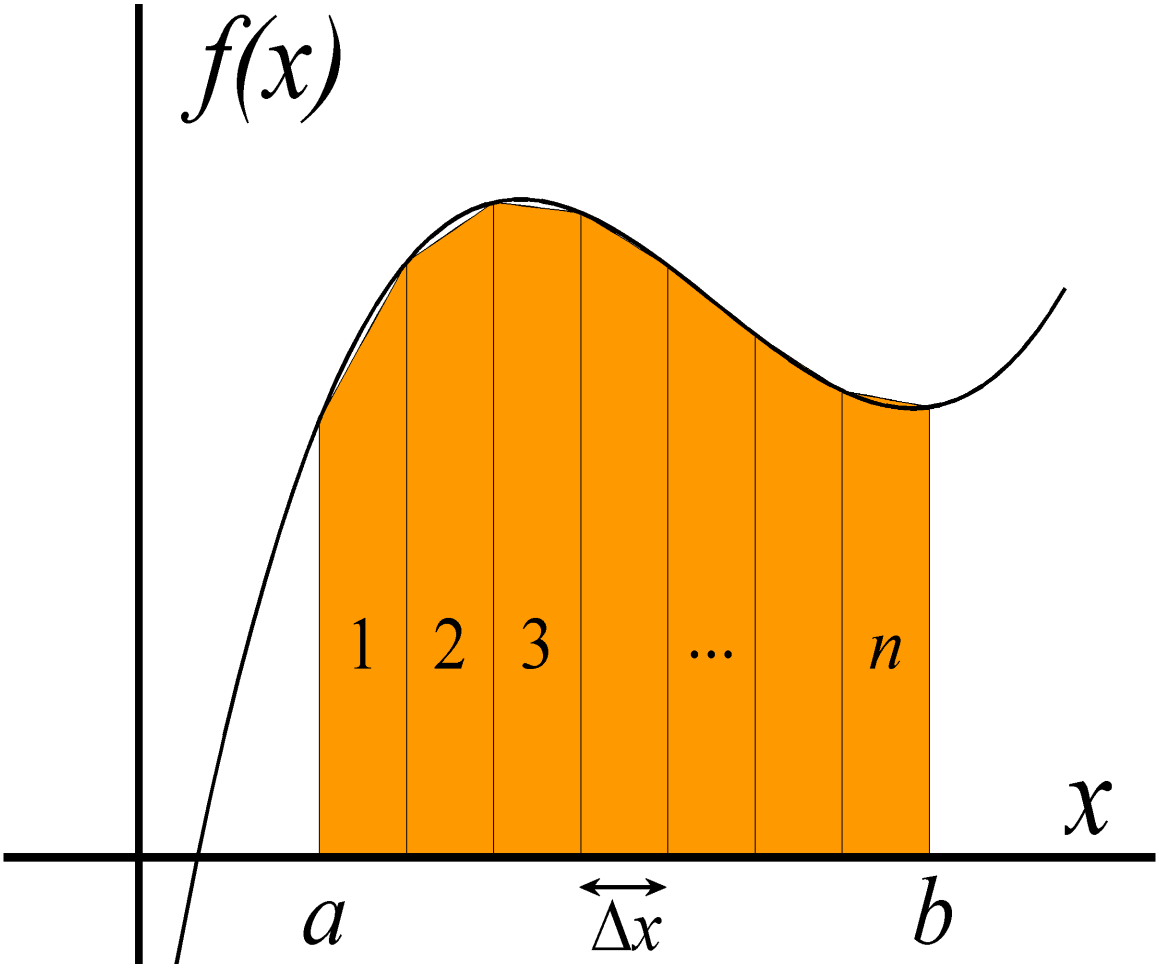

Figure D.1: 1D discretized domain. Figure taken from [70]

$$\int_a^b f(x)dx = \frac{\Delta x}{2}[f(a) + f(b) + 2(f(1) + f(2) + ...f(n-1))]. \tag{D.2}$$

2D Trapezoidal rule

Consider the discretization of a two dimensional function $f(x, y)$ in the x-y plane Fig. D.2. The integral of $f(x, y)$ between $a \leq x \leq b$ and $c \leq y \leq d$ can be interpreted as the volume V between the function in the aforementioned bounded area.

Let the step sizes in the x and y directions be Δx and Δy. Let $i = 0, 1, 2, 3, ...n$ and $j = 1, 2, 3....m$ be the indices in the x and y directions. Any arbitrary point in this 2D domain can be indexed by,

$$x_i = a + i\Delta x; y_j = c + j\Delta y. \tag{D.3}$$

The volume of each of these 3D trapezoidal elements is given by,

$$V_{ij} = \frac{1}{4}\Delta x\Delta y[f(x_{i-1}, y_{j-1}) + f(x_{i-1}, y_j) + f(x_i, y_{j-1}) + f(x_i, y_j)]. \tag{D.4}$$

The effective volume V' can be found by summing over all the volume elements and is given by,

$$V' = \frac{\Delta x\Delta y}{4}[f(a, c) + f(a, d) + f(b, c) + f(b, d)] + \frac{1}{2}\Delta x\Delta y[\sum_{i=1}^{n-1} f(x_i, c)+$$
$$\sum_{i=1}^{n-1} f(x_i, d) + \sum_{j=1}^{m-1} f(a, y_j) + \sum_{i=1}^{m-1} f(b, y_j)] + \Delta x\Delta y\sum_{i=1}^{n-1}\sum_{j=1}^{m-1} f(x_i, y_j). \tag{D.5}$$

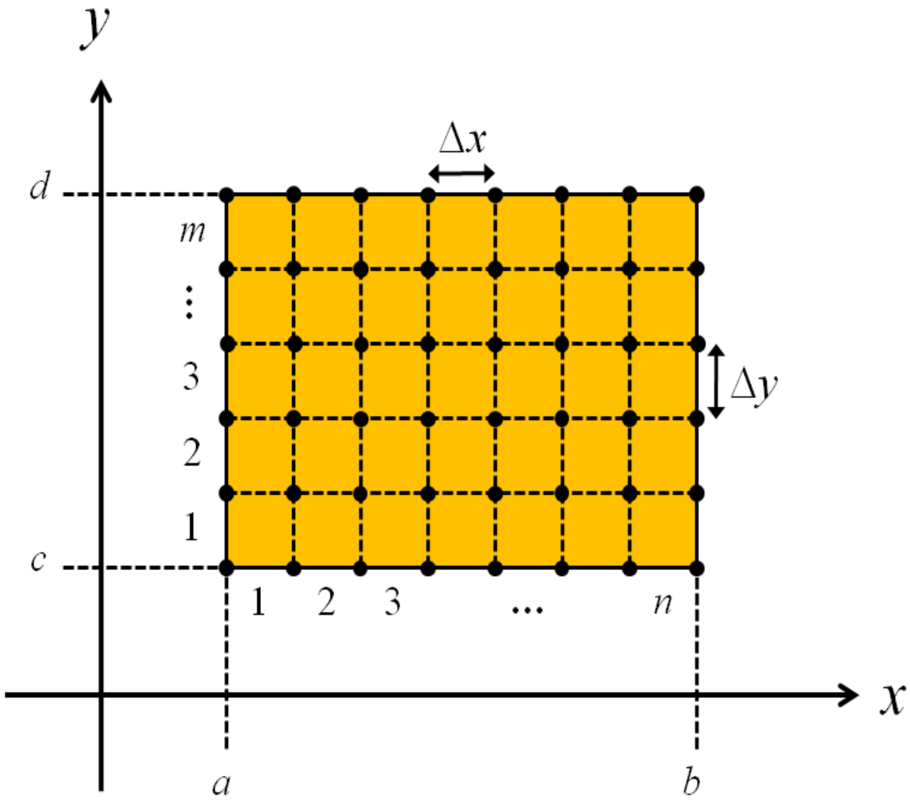

Figure D.2: 2D discretized domain. Figure taken from [70]